A Transiting Super-Earth in the Radius Valley and an Outer Planet Candidate Around HD 307842

Xinyan Hua[1] 📵, Sharon Xuesong Wang[1] 📵, Johanna K. Teske[2], Tianjun Gan[1] 📵, Avi Shporer[3] 📵, George Zhou[4] 📵,
Keivan G. Stassun[5] 📵, Markus Rabus[6] 📵, Steve B. Howell[7] 📵, Carl Ziegler[8], Jack J. Lissauer[9] 📵, Joshua N. Winn[10] 📵,
Jon M. Jenkins[7] 📵, Eric B. Ting[7] 📵, Karen A. Collins[11] 📵, Andrew W. Mann[12] 📵, Wei Zhu[1], Su Wang[13] 📵, R. Paul Butler[2] 📵,
Jeffrey D. Crane[14] 📵, Stephen A. Shectman[14] 📵, Luke G. Bouma[15] 📵, César Briceño[16] 📵, Diana Dragomir[17] 📵, William Fong[3] 📵,
Nicholas Law[12] 📵, Jennifer V. Medina[18] 📵, Samuel N. Quinn[11] 📵, George R. Ricker[3] 📵, Richard P. Schwarz[11] 📵,
Sara Seager[3,19,20] 📵, Ramotholo Sefako[21] 📵, Chris Stockdale[22] 📵, Roland Vanderspek[3] 📵, and Joel Villaseñor[3]

[1] Department of Astronomy, Tsinghua University, Beijing 100084, People's Republic of China; huaxinyan1996@gmail.com, sharonw@tsinghua.edu.cn
[2] Earth and Planets Laboratory, Carnegie Institution for Science, 5241 Broad Branch Road, NW, Washington, DC 20015, USA
[3] Department of Physics and Kavli Institute for Astrophysics and Space Research, Massachusetts Institute of Technology, Cambridge, MA 02139, USA
[4] Centre for Astrophysics, University of Southern Queensland, Queensland, Australia
[5] Department of Physics and Astronomy, Vanderbilt University, Nashville, TN 37235, USA
[6] Departamento de Matemática y Física Aplicadas, Facultad de Ingeniería, Universidad Católica de la Santísima Concepción, Alonso de Rivera 2850, Concepción, Chile
[7] NASA Ames Research Center, Moffett Field, CA 94035, USA
[8] Department of Physics, Engineering and Astronomy, Stephen F. Austin State University, 1936 North Street, Nacogdoches, TX 75962, USA
[9] Space Science & Astrobiology Division, MS 245-3, NASA Ames Research Center, Moffett Field, CA 94035, USA
[10] Department of Astrophysical Sciences, Princeton University, 4 Ivy Lane, Princeton, NJ 08544, USA
[11] Center for Astrophysics | Harvard & Smithsonian, 60 Garden Street, Cambridge, MA 02138, USA
[12] Department of Physics and Astronomy, The University of North Carolina at Chapel Hill, Chapel Hill, NC 27599-3255, USA
[13] Purple Mountain Observatory, No.10 Yuanhua Road, Nanjing 210023, People's Republic of China
[14] Observatories of the Carnegie Institution for Science, 813 Santa Barbara Street, Pasadena, CA 91101, USA
[15] Cahill Center for Astrophysics, California Institute of Technology, Pasadena, CA 91125, USA
[16] Cerro Tololo Inter-American Observatory, Casilla 603, La Serena, Chile
[17] Department of Physics and Astronomy, University of New Mexico, 210 Yale Boulevard NE, Albuquerque, NM 87106, USA
[18] Space Telescope Science Institute, 3700 San Martin Drive, Baltimore, MD, 21218, USA
[19] Department of Earth, Atmospheric, and Planetary Sciences, Massachusetts Institute of Technology, Cambridge, MA 02139, USA
[20] Department of Aeronautics and Astronautics, Massachusetts Institute of Technology, Cambridge, MA 02139, USA
[21] South African Astronomical Observatory, P.O. Box 9, Observatory, Cape Town 7935, South Africa
[22] Hazelwood Observatory, Australia

Abstract

We report the confirmation of a TESS-discovered transiting super-Earth planet orbiting a mid-G star, HD 307842 (TOI-784). The planet has a period of 2.8 days, and the radial velocity (RV) measurements constrain the mass to be $9.67^{+0.83}_{-0.82}\,M_\oplus$. We also report the discovery of an additional planet candidate on an outer orbit that is most likely nontransiting. The possible periods of the planet candidate are approximately 20–63 days, with the corresponding RV semiamplitudes expected to range from 3.2 to 5.4 m s^{-1} and minimum masses from 12.6 to 31.1 $M_\oplus$. The radius of the transiting planet (planet b) is $1.93^{+0.11}_{-0.09}\,R_\oplus$, which results in a mean density of $7.4^{+1.4}_{-1.2}$ g cm^{-3} suggesting that TOI-784 b is likely to be a rocky planet though it has a comparable radius to a sub-Neptune. We found TOI-784 b is located at the lower edge of the so-called "radius valley" in the radius versus insolation plane, which is consistent with the photoevaporation or core-powered mass-loss prediction. The TESS data did not reveal any significant transit signal of the planet candidate, and our analysis shows that the orbital inclinations of planet b and the planet candidate are $88.60^{\circ+0.84}_{-0.86}$ and $\leqslant 88^\circ.3$–$89^\circ.2$, respectively. More RV observations are needed to determine the period and mass of the second object, and search for additional planets in this system.

Unified Astronomy Thesaurus concepts: Exoplanet astronomy (486); Radial velocity (1332); Transit photometry (1709); Super Earths (1655)

Supporting material: machine-readable table

1. Introduction

Planets in extrasolar systems are common in the universe. In the past few decades, over 5000 exoplanets were discovered and confirmed. NASA's Kepler space telescope discovered thousands of transiting planet candidates with most of them having a size between Earth and Neptune (Borucki et al. 2010). Fulton et al. (2017) studied the size distribution of 2025 Kepler planets (the California–Kepler Survey (CKS) sample) in fine detail and found a bimodal structure with a gap near 1.5–2.0 $R_\oplus$ separating super-Earths and sub-Neptunes, which is referred as the "radius valley." Weiss et al. (2018) further claimed that this valley also exists in multiplanet systems.

The formation process of the radius valley and its position as a function of other planetary or host stars' parameters are still under debate. A positive relationship between the transition

radius and planet insolation flux was derived from the CKS sample (Martinez et al. 2019; Petigura et al. 2022), which can be explained by the photoevaporation scenario (e.g., Owen & Wu 2017; Fulton & Petigura 2018; Lopez & Rice 2018), where the close-in planets become stripped cores while the outer ones can keep their gas envelopes and thus have larger sizes. On the other hand, Cloutier & Menou (2020) estimated an opposite correlation using 275 Kepler and 53 K2 planets around M- and K-type stars, which is consistent with gas-poor formation theory (e.g., Lopez & Rice 2018), where most rocky planets are formed after the disks dissipate and thus without initial gaseous envelopes.

Radial velocity (RV) follow-up observations of planets with sizes near the radius valley could shine more light on the structure and origin of the valley, especially for the "keystone" planets where different models predict different fractions of volatiles (e.g., Cloutier & Menou 2020; Cloutier et al. 2020). The mass measurements from RVs would provide some constraints on the bulk composition of transiting planets, thus revealing how planetary composition might shift across the radius valley (e.g., Luque & Pallé 2022). Obtaining precise mass measurements of super-Earths and sub-Neptunes is also important for reliably characterizing the compositions of their atmospheres (if any; Batalha et al. 2019).

In addition to mass and bulk density measurements, RV follow up can also reveal additional planets in the system, either nontransiting or yet to be detected by transits, which is more important for mapping out the system architecture for transiting planets discovered by the Transiting Exoplanet Survey Satellite (TESS; Ricker et al. 2015), given its relatively shorter baseline compared with Kepler. Studies of planet multiplicity found that multiplanet systems are common (e.g., 40% among systems with super-Earths or sub-Neptunes discovered by Kepler; Batalha et al. 2013), so RV follow-up observations of transiting planets often turn out to be fruitful (e.g., Lacedelli et al. 2021; Lubin et al. 2022). Revealing the nontransiting planets in systems with single transiting planets can be of particular interest, as it directly addresses the previously identified "Kepler dichotomy," where a surplus of Kepler single-transiting systems was inconsistent with predictions from earlier population synthesis models with relatively low mutual inclinations, but consistent with an additional population of multiplanet systems with large mutual inclinations (e.g., Lissauer et al. 2011; Hansen & Murray 2013; Ballard & Johnson 2016). This "dichotomy" appears to hold for both M dwarfs and Sun-like stars, and it cannot be fully explained by selection biases (e.g., Zink et al. 2019). Different scenarios were proposed to explain the Kepler dichotomy (e.g., Mulders et al. 2018; Zhu et al. 2018; He et al. 2019, 2020), but the intrinsic mutual inclination distribution for multiplanet systems still remains uncertain. More samples of well-characterized multiplanet systems, either with RVs or transit-timing variations (TTVs), are needed for investigations on the intrinsic mutual inclination distribution of planets and studies of system architectures in general (e.g., see the review by Weiss et al. 2022).

In this work, we report a TESS-discovered transiting super-Earth, TOI-784 b, and an additional Neptune-mass planet candidate in the system using RV follow-up data taken by the Magellan TESS Survey (MTS; Teske et al. 2021). We organize this paper as follows: we first describe our observational data and data reduction processes in Section 2, as well as results

from direct imaging. We then introduce the stellar characterization in Section 3. Section 4 presents the detailed photometry and RV modeling to constrain the planetary properties. We discuss our results and present our conclusions in Section 5.

2. Observations

2.1. Photometry

2.1.1. TESS

The TESS mission is an all-sky survey primed to discover transiting exoplanets (Ricker et al. 2015), with a field of view of $24° × 96°$, observing in sectors each lasting about 27 days. From 2018 July to 2020 July, TESS mapped almost the whole sky in its two-year Primary Mission and then reobserved the southern ecliptic hemisphere during Year 3 (2020 July–2021 July) for its first Extended Mission. TESS recently completed its first Extended Mission slightly over four years from the start of science observations in 2018 July and has now commenced its second Extended Mission.

HD 307842 (TIC 460984940, hereafter TOI-784) was observed by the TESS mission and announced as TOI-784 after its Cycle 1 observation in Sectors 10 (2019 March 26–April 22) and 11 (2019 April 22–May 21) with a two minute cadence using camera 3. In Cycle 3, TOI-784 was revisited with the same mode in Sectors 37 (2021 April 2–April 28) and 38 (2021 April 28–May 26). The raw photometric data were first reduced by the Science Processing Operations Center (SPOC; Jenkins et al. 2016) pipeline at the NASA Ames Research Center, which extracted the light curve using Simple Aperture Photometry (SAP) and further calibrated for instrument systematics using the Presearch Data Conditioning (PDC) algorithm.

The SPOC Transiting Planet Search (TPS; Jenkins 2002; Jenkins et al. 2010, 2020) of the light curve via an adaptive, noise-compensating matched filter revealed a transit signal with a 2.8 day period on 2019 May 23. An initial limb-darkened transit model was fitted (Li et al. 2019) and a suite of diagnostic tests were conducted to help make or break the planetary nature of the signal(s) (Twicken et al. 2018) presented in the Data Validation reports available on the Mikulski Archive for Space Telescopes[23] (MAST). In this case the transit signal failed the ghost diagnostic test, but visual inspection of the difference images indicates that the transit source is located on the target. The TESS Science Office reviewed the vetting reports and issued an alert for TOI-784 b on 2019 June 5 (Guerrero et al. 2021).

The PDCSAP light curve file (PDCSAP flux; Smith et al. 2012; Stumpe et al. 2012, 2014) used for the photometric analyses in this work (see Section 4.1) was downloaded from MAST using the `lightkurve` package (Lightkurve Collaboration et al. 2018).

2.1.2. Las Cumbres Observatory: Sinistro

We collected three sets of ground-based light curves for TOI-784 using the Las Cumbres Observatory Global Telescope (LCOGT[24]) network (Brown et al. 2013) on 2020 February 26, 2020 March 13, and 2021 January 21 to refine the transit ephemeris and rule out the nearby eclipsing binary
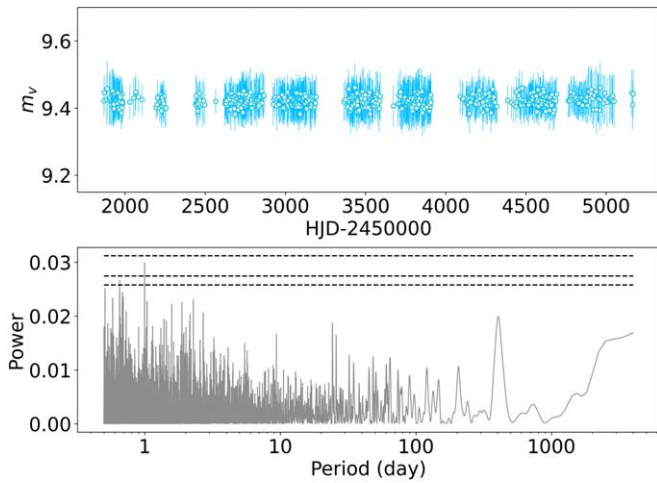
---

[23] https://archive.stsci.edu
[24] https://lco.global/

Figure 1. The ASAS *V*-band photometry (top) and its GLS periodogram. The three dashed lines from top to bottom in the lower panel correspond to 1%, 5%, and 10% significance threshold levels, respectively. The maximum signal appears at around 1 day, which is likely an alias due to the observing cadence. No significant signal was identified for the stellar rotation.

scenario. We used the `TESS Transit Finder`, which is a customized version of the `Tapir` software package (Jensen 2013), to schedule the transit observation. All three observations were taken with the Sinistro cameras in the Pan-STARRS *z*-short band (z_s) with exposure times of 70, 70, and 30 s. We carried out a photometric analysis and extracted the light curves using `AstroImageJ` (Collins et al. 2017). We excluded all nearby stars within 2″.5 of the source that may cause the TESS signal to have a brightness difference down to $\Delta T \sim 9.5$ mag and tentatively detected the signal on target. The data are publicly available on ExoFOP.[25]

2.1.3. Other Archival Ground-based Photometry

We found 963 *V*-band archival measurements of TOI-784 from the ASAS database[26] spanning from 2000 November 21 to 2009 December 3.[27] Following the ASAS documentation, we selected 883 data points ranked as grades A and B, which represent the highest-quality measurements. We applied a 3σ clipping rejection, after which 35 measurements were masked and 848 were left. Considering the *V* magnitude of our target ($\sim$9.4) and the observing aperture scale, the data points marked as "MAG_3" were used in our analysis as recommended by ASAS.[28] We calculated the generalized Lomb–Scargle (GLS) periodogram using the python module `PyAstronomy. pyTiming.pyPeriod.Gls()` to search for the rotation signal of the host star.[29] The results are shown in Figure 1: the three black dashed lines from top to bottom in the figure correspond to false-alarm probabilities (FAPs) of 1%, 5%, and

10%, which means that there is a 1%, 5%, or 10% chance, respectively, that the observed signal is a false positive. The FAP values were computed via the default function within the `Gls()` module with the default normalization assumption described in Zechmeister & Kürster (2009). We found no significant rotation modulation, suggesting that TOI-784 is probably an old, slowly rotating, and photometrically quiet star. The peak around one day is likely an alias resulting from the observation cadence.

2.2. Spectroscopy

2.2.1. PFS

We collected a total of 35 RV data points using the Planet Finder Spectrograph (PFS; Crane et al. 2006, 2008, 2010) on the 6.5 m Magellan II Clay telescope at Las Campanas Observatory in Chile. PFS is a high-resolution, optical echelle spectrograph that covers a wavelength band of 391–734 nm with a resolving power of $R \sim 130{,}000$ using the 0″.3 × 2″.5 slit. The RV precision of PFS on nearby, bright, and photospherically quiet stars is typically 0.5–1.0 m s^{-1}. The spectral data reduction and RV extraction were performed using a customized pipeline (Butler et al. 1996).

Our PFS data were obtained as part of the MTS (Teske et al. 2021), a project designed to study a sample of 30 well-characterized small planets with radii $< 3 R_\oplus$ to reveal their population statistics such as the mass–radius (M–R) relation (Wolfgang et al. 2016; Weiss et al. 2018), the "radius gap" around $1.8 R_\oplus$ (Fulton et al. 2017; Petigura et al. 2022), and other stellar properties/system architectures in order to reveal their formation and evolution processes. A sample of 30 targets were selected using a quantified merit function among the TESS Objects of Interest (TOIs) from the Year 1 observations of TESS (therefore only includes the southern hemisphere), and TOI-784 was among the initial sample of 30 at the beginning of the MTS but later on dropped off the list due to the refinement of the stellar and planetary parameters of the TOIs over time.

The MTS adopts a specific observing strategy to minimize selection bias (see Teske et al. 2021 for more details about the observing cadence design). TOI-784 received a High Cadence grade for its coverage, with 22 RV observations taken from UT March 6 to UT March 17 in 2020 and nine RV data points between UT May 22 and UT May 29 in 2021, and MTS stopped observing TOI-784 afterward as it dropped off of the target list. We then collected four more data points from UT 2022 Match 14 to 2022 March 25 in order to characterize the additional long-period planet candidate, as the RV fitting results using the first year's data showed a linear trend in the residuals (see Section 4.2 for more). With a typical exposure time of 10–20 minutes depending on the seeing, the reported internal RV precision $\sigma_{\rm RV}$ of PFS on TOI-784 is 0.7–1.0 m s^{-1}. See Table 1 for all the PFS RVs used in this work.

2.2.2. NRES

We acquired TOI-784 spectra using LOC's Network of Robotic Echelle Spectrographs (NRES; Siverd et al. 2018). LCO-NRES consists of four high-resolution optical echelle spectrographs (located in Chile, South Africa, Israel, and USA) with a resolution of $R \sim 53{,}000$ and a wavelength range spanning 380–860 nm. Each spectrograph is fed by two fibers: one fiber is illuminated by the stellar light coming from a 1 m telescope at the respective site, and the second one is fed by a

---

[25] https://exofop.ipac.caltech.edu/tess/target.php?id=88902249

[26] http://www.astrouw.edu.pl/asas/?page=aasc&catsrc=asas3

[27] We also found archival photometry data from ASAS-SN (https://asas-sn. osu.edu/photometry), in which we saw a long term trend spanning the temporal baseline ($\sim$904 days), so we did not adopt it. We found no archival data from WASP (https://wasp.cerit-sc.cz/form).

[28] Indices from 0 to 4 indicate five apertures of 2–6 pixels wide. Small ones are better for faint stars while large ones for bright stars, roughly following the relation of aperture index $= 12 - V$. See http://www.astrouw.edu.pl/asas/explanations.html for more detailed explanations.

[29] A same analysis was applied using the TESS light curve, which alerted no evident signal as expected.

Table 1
RV Measurements

Time	RV (m s^{-1})	Uncertainty (m s^{-1})	Instrument
2458914.68102	−6.02	0.83	PFS
2458914.80040	−8.24	0.87	PFS
2458915.68459	−3.32	0.79	PFS
2458915.75693	−3.82	0.78	PFS
2458916.71986	0.34	0.77	PFS
2458917.65647	−6.89	0.74	PFS
2458917.73457	−5.19	0.74	PFS
2458918.67521	0.27	0.91	PFS
2458918.75249	2.39	0.72	PFS
2458919.66161	0.12	0.68	PFS
2458919.74236	3.05	0.70	PFS
2458920.65817	−5.21	0.64	PFS
2458920.71749	−4.78	0.64	PFS
2458921.67109	3.56	0.65	PFS
2458921.73069	6.03	0.62	PFS
2458923.63457	−0.01	0.71	PFS
2458923.70633	−1.72	0.75	PFS
2458924.62670	6.63	0.61	PFS
2458924.70608	6.77	0.70	PFS
2458924.77554	8.45	0.72	PFS
2458925.62948	1.55	0.67	PFS
2458925.71178	−0.09	0.72	PFS
2459356.50045	−6.68	0.99	PFS
2459356.57079	−6.90	1.06	PFS
2459358.57198	0.90	1.09	PFS
2459359.49081	−6.39	1.11	PFS
2459359.58574	−8.32	1.03	PFS
2459361.45964	0.80	1.03	PFS
2459361.58363	0.59	1.14	PFS
2459363.46677	3.25	1.08	PFS
2459363.55417	5.02	1.04	PFS
2459652.72417	−0.57	0.73	PFS
2459654.70344	2.93	0.70	PFS
2459657.67591	0.00	0.71	PFS
2459663.67738	−1.96	1.00	PFS
2459336.22205515	15,163.8	10.5	NRES1
2459344.41512404	15,157.3	9.1	NRES1
2459346.23537912	15,136.2	9.2	NRES1
2459348.25530748	15,198.2	9.0	NRES1
2459353.21427107	15,118.7	9.4	NRES1
2459357.35987432	15,162.1	11.0	NRES1
2459360.33375668	15,153.9	9.8	NRES1
2459369.30694576	15,142.5	8.7	NRES1
2459376.32741634	15,122.2	8.9	NRES1
2459377.24338348	15,102.5	8.9	NRES1
2459411.24579787	15,080.6	8.1	NRES1
2459578.74273868	14,871.4	5.7	NRES2
2459580.74290906	14,877.7	5.5	NRES2
2459584.74664902	14,918.7	5.3	NRES2
2459593.79187993	14,922.3	9.0	NRES2
2459597.72988968	14,834.6	7.9	NRES2
2459601.75295545	14,930.1	8.5	NRES2
2459602.75137792	14,925.8	6.8	NRES2
2459604.79780727	14,882.6	6.4	NRES2
2459609.68250136	14,854.9	4.9	NRES2
2458909.692940	15,780.0	27.0	CHIRON
2458916.735210	15,743.0	24.0	CHIRON
2459428.457080	15,786.0	20.0	CHIRON

(This table is available in machine-readable form.)

ThAr reference lamp. At the beginning of each night, each NRES unit automatically takes calibration images including bias, dark, flat, and ThAr frames.

We randomly scheduled our observations with a time span of 1–4 days to avoid any observing bias (Burt et al. 2018) and constrained the lunar separation threshold to 30° and the airmass to <1.6. Our exposure times ranged from 30 to 40 minutes, reaching a signal-to-noise ratio (S/N) between 40 and 90 at 5130 Å. We collected 12 spectra in total from 2021 May to July on the NRES unit in South Africa (CPT) and 18 spectra from 2021 December to 2022 January on the unit in Chile (LSC). After binning multiple shots taken on the same nights to enhance the S/N, we ended up with 20 RV data points from LCO-NRES. The raw spectra were calibrated and wavelength corrected using the CERES pipeline (Brahm et al. 2017). By cross-correlating the observed spectra with a binary mask, the CERES pipeline also delivers RV measurements for each spectrum. The reported internal RV precision on TOI-784 is typically around 10 m s^{-1}. See Table 1 for all the NRES RVs.

2.2.3. CHIRON

We obtained three observations of TOI-784 via the CHIRON facility between 2020 March and 2021 August to provide reconnaissance spectroscopic vetting of the target. CHIRON is a fiber-fed high-resolution echelle spectrograph at the SMARTS 1.5 m telescope located at Cerro Tololo Inter-American Observatory, Chile (Tokovinin et al. 2013) with a spectral coverage of 410–870 nm. TOI-784 was observed in the fiber mode, with a spectral resolving power of $R \sim 28,000$ and an exposure time of 5 minutes. The RV precision is about 20–30 m s^{-1}. The spectra were extracted through the official CHIRON pipeline described in Paredes et al. (2021). We derived RVs from a least squares deconvolution between each observation and a nonrotating synthetic template, which is generated via the ATLAS9 atmosphere models (Castelli & Kurucz 2003) at the given spectral parameters of the targets. The derived broadening profile is fitted with a kernel accounting for the effects of rotation, macroturbulence, instrumental broadening, and RV shift. The CHIRON spectra were also used to estimate the stellar parameters, which are described in detail in Section 3.2. The CHIRON RVs are listed in Table 1.

2.3. High-Resolution Speckle Imaging

Spatially close stellar companions can create false-positive transit signals and/or lessen the transit depth, causing the exoplanet's radius to be underestimated. Thus, determination of the "third-light" flux contamination from the close companion stars is important to account for properly or rule out. To search for close-in bound (or line of sight) companions unresolved in the TESS or other ground-based follow-up observations, we obtained high-resolution imaging speckle observations of TOI-784.

2.3.1. SOAR HRcam

We searched for stellar companions to TOI-784 with speckle imaging on the 4.1 m Southern Astrophysical Research (SOAR) telescope (Tokovinin 2018) on 2019 July 14 UT, observing in Cousins I band, a similar visible bandpass as used by TESS. This observation was sensitive to a 5.4 mag or fainter star at an angular distance of 1″ from the target. More details of the observations within the SOAR TESS survey are available in Ziegler et al. (2020). The 5σ detection sensitivity and speckle
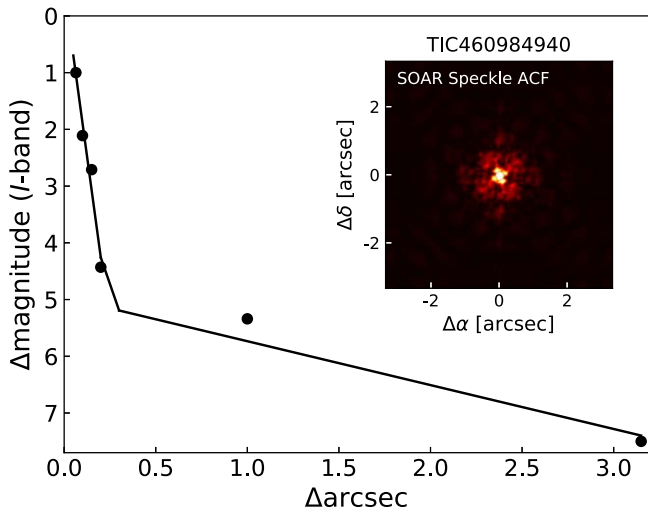
Figure 2. SOAR high-resolution speckle image contrast limits in the Cousins *I* bandpass. The inserts show the speckle auto-correlation function. SOAR did not detect a nearby companion to TOI-784.

auto-correlation functions from the observations are shown in Figure 2. No nearby stars were detected within 3″ of TOI-784 in the SOAR observations.

2.3.2. Gemini Zorro

TOI-784 was observed on 2020 March 12 UT using the Zorro speckle instrument on the Gemini South 8 m telescope.[30] Zorro provides simultaneous speckle imaging in two bands (562 and 832 nm) with output data products including a reconstructed image with robust contrast limits on companion detections. Three sets of 1000×0.06 s exposures were collected and subjected to Fourier analysis in our standard reduction pipeline (see Howell et al. 2011). Figure 3 shows our final contrast curves and our reconstructed speckle images. We find that TOI-784 is a single star with no companion brighter than 5–9 magnitudes below that of the target star from the diffraction limit (20 mas) out to 1″2. At the distance of TOI-784 ($d = 64.6$ pc) these angular limits correspond to spatial limits of 1.3–77.5 au.

3. Stellar Characterization

3.1. Spectral Energy Distribution

As an independent check on the fundamental parameters of the host star, we carry out an analysis of the broadband spectral energy distribution (SED) together with the Gaia EDR3 parallax in order to determine an independent, empirical measurement of the stellar radius, following the procedures described in Stassun & Torres (2016), Stassun et al. (2017), and Stassun & Torres (2018). We pull the *BV* magnitudes from Mermilliod (2006), the $B_T V_T$ magnitudes from Tycho-2, the JHK_S magnitudes from the Two Micron All Sky Survey (2MASS), the W1–W4 magnitudes from the Wide-field Infrared Survey Explorer (WISE), and the three Gaia magnitudes G, G_{BP}, and G_{RP}. Together, the available photometry spans the full stellar SED over the wavelength range 0.4–22 μm (see Figure 4).

---

[30] https://www.gemini.edu/sciops/instruments/alopeke-zorro/
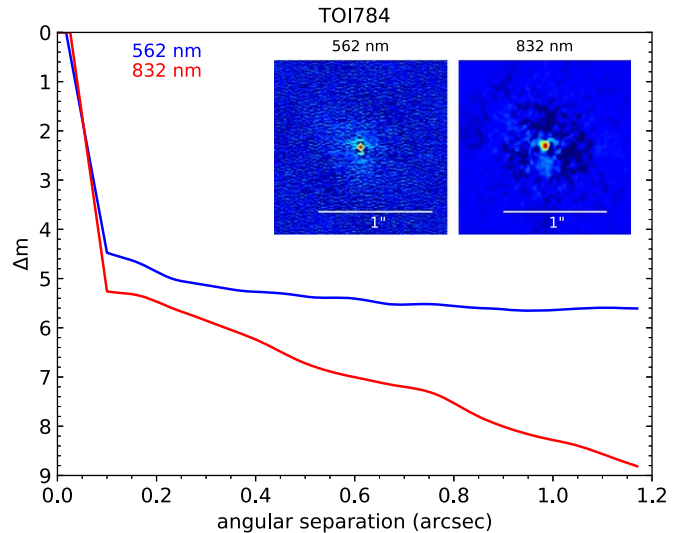

Figure 3. Zorro high-resolution speckle image contrast limits in both 562 and 832 nm bandpasses. The inserts show the reconstructed images in both bandpasses, highlighting that TOI-784 is a single star to the contrast levels achieved (1.3–77.5 au).

We perform a fit using Kurucz stellar atmosphere models, with $T_{\rm eff}$, $\log g$, and [Fe/H] taken from the spectroscopic analysis (see below). The remaining parameter is the extinction (A_V), which we constrained to be no larger than the full line-of-sight extinction from the dust maps of Schlegel et al. (1998). The resulting fit is shown in Figure 4 with a reduced χ^2 of 1.2 and a best-fit extinction of $A_V = 0.15 \pm 0.03$ mag. Integrating the model SED gives the bolometric flux at Earth of $F_{\rm bol} = 5.423 \pm 0.063 \times 10^{-9}$ erg s^{-1} cm^{-2}. Taking the $F_{\rm bol}$ and $T_{\rm eff}$ together with the Gaia parallax, with no adjustment for systematic parallax offset (see, e.g., Stassun & Torres 2021), gives the stellar radius as $R_\star = 0.907 \pm 0.017\,R_\odot$. We can also estimate the stellar mass empirically via $R_\star$ together with the spectroscopic $\log g$, which gives $M_\star = 0.91 \pm 0.10\,M_\odot$, and which is consistent with the value of $0.95 \pm 0.06\,M_\odot$ inferred from the empirical relations of Torres et al. (2010).

Finally, using $R_\star$ together with the spectroscopically estimated rotational velocity ($v \sin i$; see below), we can infer the stellar rotation period, which gives $P_{\rm rot}/\sin i = 41.7 \pm 11.4$ days. That rotation period yields an estimated system age via empirical gyrochronology relations (Mamajek & Hillenbrand 2008) of 7.8 ± 3.4 Gyr. We caution the readers that the rotation period and age estimates are both based on the poorly constrained $v \sin i$ value from spectroscopy, and thus they serve as only a rough check to confirm that TOI-784 is an old star. We summarize the basic information of HD 307842 in Table 2.

3.2. Spectroscopic Parameters

To estimate the stellar parameters of TOI-784, we followed Zhou et al. (2020) and compared the CHIRON spectra against those in a library of ~10,000 observed spectra previously classified via the Spectroscopic Classification Pipeline (SPC; Buchhave et al. 2012). The library is interpolated via a gradient-boosting regressor implemented in the scikit-learn package. We found a best-fit effective temperature of 5558 ± 100 K, surface gravity of $\log g_\star = 4.48 \pm 0.10$, and metallicity of [Fe/H] $= -0.13 \pm 0.08$ for TOI-784. The standard deviation from the stellar parameters derived from each spectrum are very small (31 K, 0.03 dex, and 0.03 dex,
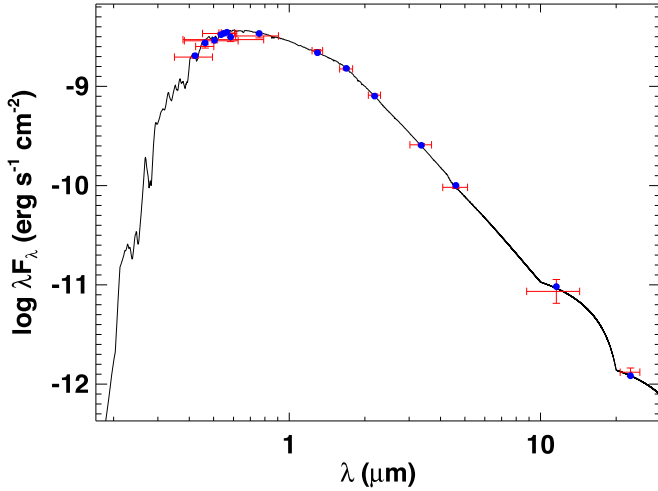
Figure 4. The best SED fit for TOI-784. Red symbols represent the observed photometric measurements, where the horizontal bars represent the effective width of the bandpass. Blue symbols are the model fluxes from the best-fit Kurucz atmosphere model (black solid line; Kurucz 1979; Castelli & Kurucz 2003).

Table 2
Basic Information of HD 307842

Parameter	Value	Description
TIC ID[1]	460984940	TESS Input Catalog
TOI ID[1]	784	TESS Object of Interest
R.A. (J2000)[2]	$10^h37^m21\overset{s}{.}88$	R.A.
Decl. (J2000)[2]	$-63°39'18''09$	decl.
μ_α (mas yr^{-1})[2]	3.413 ± 0.012	Proper motion
μ_δ (mas yr^{-1})[2]	-154.788 ± 0.011	Proper motion
ϖ (mas)[2]	15.4833 ± 0.0108	Parallax distance
D (pc)[2]	64.59 ± 0.05	Stellar distance
RV (km s^{-1})[3]	15.06 ± 0.66	RV
$T_{\rm eff}$ (K)[4]	5558 ± 100	Effective temperature
$\log g_\star$ (dex)[4]	4.48 ± 0.10	Surface gravity
[Fe/H] (dex)[4]	-0.13 ± 0.08	Stellar metallicity
$v \sin i$ (km s^{-1})[4]	$\lesssim 1.1 \pm 0.3$	Rotation speed
T[1]	8.705 ± 0.017	T-band magnitude
V[1]	9.412 ± 0.003	V-band magnitude
$\log R'_{\rm HK}$[4]	-4.99	
$R_\star$ ($R_\odot$)[4]	0.907 ± 0.017	Stellar radius
$M_\star$ ($M_\odot$)[4]	0.91 ± 0.10	Stellar mass

Note. References: (1) Guerrero et al. (2021); (2) Gaia Collaboration (2020); (3) Gaia Collaboration (2018); and (4) this work.

respectively), showing that the photon-limited uncertainties for the stellar parameters are significantly smaller than the associated model-dependent uncertainties. Considering that the stellar properties are relatively Sun-like where models are well calibrated, we quoted a minimum temperature error of 100 K, which is the floor systematic uncertainty ($\sim$2% in temperature) recommended in Tayar et al. (2022).

In addition to the spectroscopic atmospheric parameters, we also measured the star's projected rotational broadening velocity $v \sin i$ through a least squares deconvolution analysis. As per Section 2.2.3, the line broadening profile is modeled via a convolution of kernels describing the rotational, macro-turbulent, and instrumental broadening effects. We found that we cannot resolve the rotational broadening of the star at the given instrumental resolution, measuring a maximum

broadening of <3 km s^{-1} from the CHIRON observations. Nevertheless, we can safely conclude that the star is rotating at a rather slow speed, as we have mentioned in the GLS periodogram test of ground-based photometry, which indicates a very weak rotation signal as well (see Section 2.1.3).

Following the procedure in Lehtinen et al. (2016; their Equations (6)–(9)), we estimated the logarithmic $R'_{\rm HK}$ of TOI-784 based on the PFS spectra. There are 13 among 35 PFS spectra having valid S-index measurements and are therefore used to calibrate the final $\log R'_{\rm HK}$. An average value of -4.99 was obtained after the calculations. We then converted it to the age ($\log \tau$) of the target using Equation (3) in Mamajek & Hillenbrand (2008) and find that $\log \tau \sim 9.8$. Thus it is not surprising that TOI-784 has a low measured $v \sin i$, given that $\log R'_{\rm HK}$ falls into the "inactive" range of -5.10 to -4.75 as classified by Henry et al. (1996). The S-index has a median value of $\sim$0.180, and it exhibits little variation with a standard deviation of $\sim$0.005, further indicating that TOI-784 is an inactive star.

TOI-784 is likely to have no wide-orbiting stellar companions since we found no matches in the catalogs from Brandt (2021) or Behmard et al. (2022), which provided cross-calibrations with Hipparcos and TOIs with Gaia EDR3 to search for stellar companions.

4. Estimates of the Planetary Parameters

4.1. Photometric Analysis

4.1.1. Transit Fit

We refer to the planet candidate and its parameters with an index of "c" for convenience in the following analyses, though it is not confirmed to be a planet as our RV data do not fully cover one orbital phase.

We used the Juliet package (Espinoza et al. 2019) to model the TESS PDCSAP flux after removing all NaN values and outliers. Juliet generates a transit model via batman (Kreidberg 2015) and supports nested samplers either using the MultiNest algorithm (Feroz & Hobson 2008; Feroz et al. 2009, 2019) through either the PyMultiNest package (Buchner et al. 2014) or the dynesty package (Speagle 2019). We adopted PyMultiNest in this work.

We first fitted a Gaussian process (GP) with a Matérn kernel to the data with the transit windows masked. The adjustable parameters and their priors along with the best-fit values are listed in Table 3. The best-fit value corresponds to the median of the posterior distribution, with the lower and upper limits being defined by the 16th and 84th percentiles of the posterior distribution, respectively. The same applies throughout the rest of the paper. We set uniform priors with widths of one day for the planet orbital period (P_b) and the time of conjunction ($t_{0,b}$) according to the values provided on ExoFOP, which are wide enough to not influence the results and can save the computational time compared to infinitely wide ones. The stellar density was estimated by the SED fitting and therefore received a normal prior centered at 1719.4 kg m^{-3} with $\sigma = 212.6$. We adopted a new parameterization of $r_{1,b}$ and $r_{2,b}$ with a uniform prior between 0 and 1 to fit the planet-to-star radius ratio $p = R_b/R_\star$ and the impact parameter $b = (a_b/R_\star)\cos i_b$, which follows the relations in the algorithm proposed by Espinoza (2018). This new parameterization and sampling will explore all the physically meaningful ranges for

Table 3
Priors, Best-fit values, and Derived Parameters of the TESS Photometric Analysis

Parameter	Prior	Best-fit value	Description
Detrending parameters			
D_{TESS}	Fixed	1	TESS photometric dilution factor
M_{TESS}	$\mathcal{N}(0, 0.1^2)$	$0.00010^{+0.000096}_{-0.000094}$	Mean out-of-transit flux of the TESS photometry
σ_{TESS} (ppm)	$\mathcal{J}(10^{-6}, 10^6)$	$172.76^{+4.80}_{-4.69}$	Extra photometric jitter term of the TESS light curve
$\sigma_{\mathrm{GP,TESS}}$ (ppm)	$\mathcal{J}(10^{-6}, 10^6)$	$0.00049^{+0.000029}_{-0.000015}$	Amplitude of the GP
$\rho_{\mathrm{GP,TESS}}$	$\mathcal{J}(10^{-3}, 10^3)$	$2.52^{+0.16}_{-0.11}$	Length scale of the GP
Transit parameters			
P_b (day)	$\mathcal{U}(2.3, 3.3)$	$2.7970365^{+0.0000031}_{-0.0000030}$	Orbital period of TOI-784 b
$t_{0,b}$ (BJD − 2457000)	$\mathcal{U}(2336.1, 2337.1)$	$2336.61221^{+0.00044}_{-0.00050}$	Time-of-transit center center for TOI-784 b
$r_{1,b}$	$\mathcal{U}(0, 1)$	$0.480^{+0.081}_{-0.088}$	Parameterization for p and b
$r_{2,b}$	$\mathcal{U}(0, 1)$	$0.0195^{+0.0010}_{-0.0009}$	Parameterization for p and b
e_b	Fixed	0	Orbital eccentricity of TOI-784 b
ω_b	Fixed	90	Argument of periapsis of TOI-784 b
$\rho_\star$ (kg m^{-3})	$\mathcal{N}(1719.4, 212.6^2)$	1781^{+111}_{-178}	Stellar density
TESS photometric parameters			
$q_{1,\mathrm{TESS}}$	$\mathcal{U}(0, 1)$	$0.10^{+0.13}_{-0.07}$	Quadratic limb darkening coefficient
$q_{2,\mathrm{TESS}}$	$\mathcal{U}(0, 1)$	$0.28^{+0.35}_{-0.21}$	Quadratic limb darkening coefficient
D_{TESS}	$\mathcal{N}(1, 0.1^2)$	$0.981^{+0.090}_{-0.086}$	TESS photometric dilution factor
M_{TESS}	$\mathcal{N}(0, 0.1^2)$	$-0.0000015^{+0.0000022}_{-0.0000021}$	Mean out-of-transit flux of the TESS photometry
σ_{TESS} (ppm)	$\mathcal{J}(0.1, 1000)$	$158.8^{+5.5}_{-5.4}$	Additional photometric jitter term of TESS
Derived planetary parameters			
$a_b/R_\star$	…	$9.03^{+0.18}_{-0.31}$	Scaled semimajor axis of the orbit for TOI-784 b
b_b	…	$0.22^{+0.12}_{-0.13}$	Impact parameter of the orbit for TOI-784 b
p_b	…	$0.0195^{+0.0010}_{-0.0009}$	Planet-to-star radius ratio
i_b (°)	…	$88.60^{+0.84}_{-0.86}$	Orbital inclination of TOI-784 b

p and b in the (b, p) plane and meanwhile meet the condition of $b < 1 + p$.

We floated the eccentricity e_b and the argument of periapsis ω_b to test if the photometry could provide any constraint on the planet's eccentricity. For e_b and ω_b we gave wide, uninformative priors of $\mathcal{U}(0, 1)$ and $\mathcal{U}(0, 360°)$, respectively. No obvious evidence for an eccentric orbit was found and e_b converged toward zero with the value of $0.10^{+0.10}_{-0.07}$. The Bayesian model log-evidence $\ln Z$ between the circular and eccentric orbit models were compared following Trotta (2008). We judge whether one model is more favored than the other by considering $2 \leqslant \Delta \ln Z < 5$ as moderate evidence and $\Delta \ln Z \geqslant 5$ as strong evidence. In our case, $\ln Z$ of a circular orbit model is ~ 2.3 larger than the eccentric one. Given the small period of planet b, we also expect that tidal forces might have damped the eccentricity to below the detectable level of the TESS light curves. We thus adopted $e_b \equiv 0$.

In principle, flux contamination from other stars in the nearby pixels was already removed from the PDCSAP file, but considering the contamination ratio estimated by TICv8 is relatively large (0.1) for this target, we floated the TESS photometric dilution factor D_{TESS} with a normal prior centered around 1.0 with a standard deviation of 0.1. This parameter converged to the value of 0.98 ± 0.09, so it was then fixed to 1.0 in the following TTV analysis (Section 4.1.2). We gave uniform priors $\mathcal{U}(0, 1)$ to the quadratic limb darkening coefficients $q_{1,\mathrm{TESS}}$ and $q_{2,\mathrm{TESS}}$.

Figures 5 and 6 show our fitting results. We obtained a planet period of 2.797 days for TOI-784 b, which is consistent with the TESS-provided value. Combining with the stellar radius in Section 3.1, we derived the planet radius R_b to be $1.93^{+0.11}_{-0.09} R_\oplus$ from the best-fit values of b and p.

4.1.2. TTV Analysis

After detrending the light curves of TOI-784, we also checked if the system has TTV signals using Juliet. We applied the dynesty package this time for higher computational efficiency. There are 20 transits in the first year (2019) and 18 transits in 2021. The ninth transit observed in 2021 was partiality captured at the beginning of Sector 38, and thus was excluded in the following analyses. The planet period P_b and transit epoch $t_{0,b}$ used to calculate the ephemeris for each transit comes from the transit modeling of the TESS photometry in the previous subsection, which gives us $P_b = 2.797$ days and $t_{0,b} = 2336.6$ (BJD − 2457000). We set a normal prior for each transit ephemeris centered at the corresponding best-fitted time of conjunction with a standard deviation of 0.01. Other parameters' priors remain the same as in Section 4.1.1 except the TESS photometric dilution factor D_{TESS}, which we simply fixed to one for efficiency concerns.

We do not find any convincing evidence of TTV in our results. The O − Cs range from about 0.2 to 13.5 minutes with no periodic feature as shown in Figure 7. This is as expected given our estimates of the possible orbital solutions and mass for the planet candidate (see Section 4.2). We estimated the possible Hill radii of the candidate using the equation $r = a_c(1 - e_c)[m_c/(3M_\star)]^{1/3}$ (Hamilton & Burns 1992), and we found that the maximum Hill sphere radius of planet candidate c is $r_{H,c} \sim 0.011$ au, corresponding to only $0.041(a_c - a_b)$ given $a_b \sim 0.038$ au. The average ratio between $r_{H,c}$ and the separation of the two planets $(a_c - a_b)$ is about 0.035 over the six possible solutions of planet candidate c found in RadVel, which means that the second planet is too far away from planet b to cause any significant TTVs.
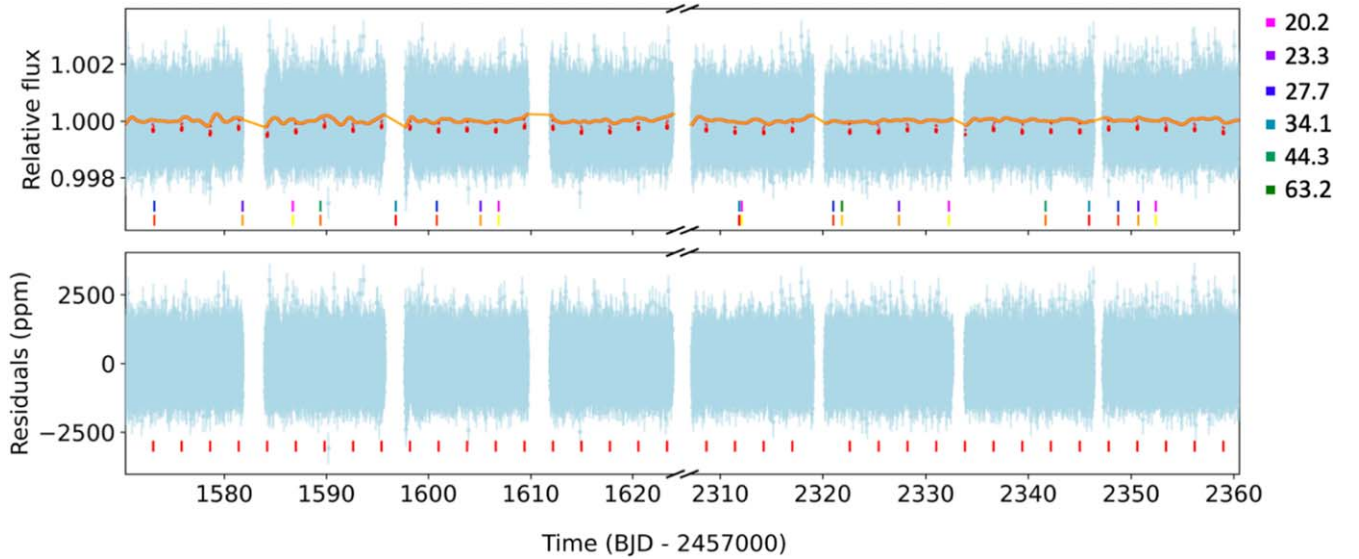
Figure 5. Top panel: TESS light curve and our best-fit detrending and transit model for planet b, with illustrations of the possible transit ephemerides of the planet candidate. The orange solid line corresponds to the detrending model using GP, while the transit fitting results are marked in red. The short vertical lines near the bottom illustrate the most probable transit ephemerides of the candidate based on the MAP grid search from RadVel (see Section 4.2.1). Each probable set of ephemerides is marked with two sets of vertical lines: the top set of magenta to cyan colors correspond to an increasing period value as labeled on the right, while the bottom set of yellow to red corresponds to an increasing MAP value. Bottom panel: residuals of the photometric fit. In this panel only the transit events of planet b are marked with small red vertical lines. Note that the time axis is not continuous as there is a 683 day gap with no TESS measurements.
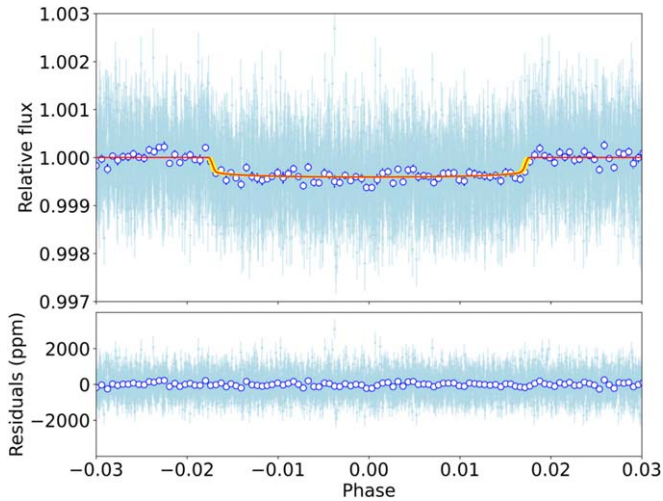
Figure 6. Phase-folded TESS light curve (light blue) and the best-fit transit model (red line with yellow 1σ band) for planet b, with the residuals plotted in the lower panel. The big circular points show the binned photometry with 40 data points in each bin.

Figure 7. $O - C$ diagram of the TTV analysis, showing the timing of the transit midpoint for each epoch. In total there were 36 transits in our TTV analysis using juliet. We found no apparent TTV signals.

4.2. RV Analysis—Possible Solutions of a Two-planet Fit

Modeling the RV data taken by Magellan/PFS with a single transiting planet leaves a clear residual beyond the estimated level of stellar jitter ($\lesssim 1.2$ m s^{-1}; see Appendix). This can be seen in Figure 16, which displays an example of the one-planet RV fit and shows clear residuals after subtracting the signals from planet b (in panel (b)). This trend is unlikely to be caused by instrumental systematics, since a significant linear trend like this, as large as $\sim$5 m s^{-1} in ten days, has not been observed in the RVs of any standard stars observed by PFS. For example, PFS's RVs of Tau Ceti (HD 10700) have a standard deviation of less than 2 m s^{-1} in four years. Therefore, we incorporated a second planet in our RV model.

We performed a joint fit of the two-year PFS data along with the NRES and CHIRON data using RadVel. However, due to the limited RV data time span, we could not map out the entire orbit of the second planet. The maximum a posteriori (MAP) solution for the second planet's orbit is quite sensitive to the specific initial guesses for its RV semiamplitude K_c and orbital period P_c, and afterward, the results of the Markov Chain Monte Carlo (MCMC) analysis will fall into local minima. As two out of three sections of the PFS data appear to capture the same phase of the second planet's orbit (see Figure 16), the degeneracy between P_c and K_c is not surprising. Therefore, we explore the parameter space for the potential second planet and provide a suite of best estimates for the orbital solution of this planet candidate.

In this section, we explore the (P_c, K_c) parameter space using both RadVel and Juliet to identify potential orbital solutions for the planet candidate. Initially, we utilized the NRES and CHIRON RVs along with the PFS RVs to place an upper limit on the RV semimajor amplitude for the planet candidate, excluding the possibility of a brown dwarf. Therefore, we took four more RV observations with PFS in 2022 March. With the new data at hand, we found that the possible solutions are primarily determined by the PFS RVs. To help the
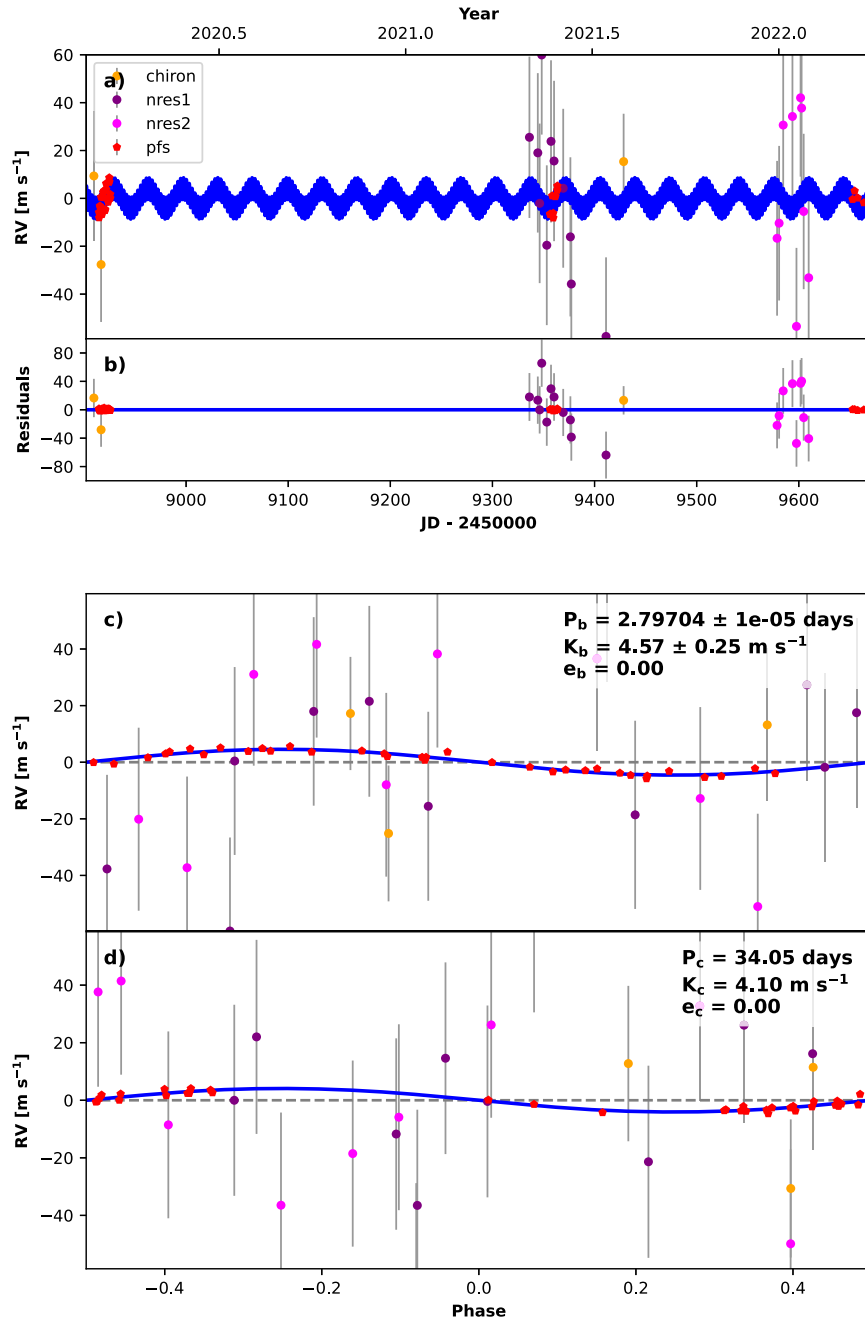
Figure 8. An example of the two-planet Keplerian orbital model. The period P_c and RV semiamplitude K_c are fixed at 34.05 days and 4.1 m s^{-1}, respectively, which is the solution with the highest MAP value among our MAP grid search (see Section 4.2.1). RVs from different instruments are marked with different colors following previous plots: red—PFS, purple and magenta—NRES (indices of 1 and 2 represent the facilities at the South African Astronomical Observatory and Cerro Tololo Inter-American Observatory, respectively), and yellow—CHIRON.

nested sampling converge in `Juliet` and simplify our model, we excluded the NRES and CHIRON RVs from the subsequent analyses.

Although we only use PFS data, we include an example of a two-planet fit that uses data from all three instruments in Figure 8 for completeness. Additionally, we present our fits assuming only planet b's signal along with some other non-Keplerian signals (such as additional RV trends or a generic GP model) in Appendix.

Table 4 presents a model comparison of different RV models using the Bayesian information criterion (BIC) and the second-order Akaike information criterion (AIC$_c$). Both BIC and AIC$_c$ are statistical model selection criteria used to assess the fit of a

model to a given data set. AIC$_c$ is a corrected version of AIC that accounts for sample size. Lower values of AIC$_c$ and BIC indicate a better model fit. According to the `RadVel` manual, we consider that we cannot distinguish the goodness of two models when ΔAIC$_c$ is less than 2; we consider that one is slightly more favored with ΔAIC$_c$ between 2 and 4; we consider that one is strongly disfavored with ΔAIC$_c$ between 4 and 10; and we consider that one can be ruled out when ΔAIC$_c$ is greater than 10. Using these criteria, we compared the one-planet fit assuming a circular or eccentric orbit for planet b and found that the former is more favored. Thus, we applied the circular orbit and compared the one-planet fit versus the two-planet fit. We will discuss the two-planet fit in the following
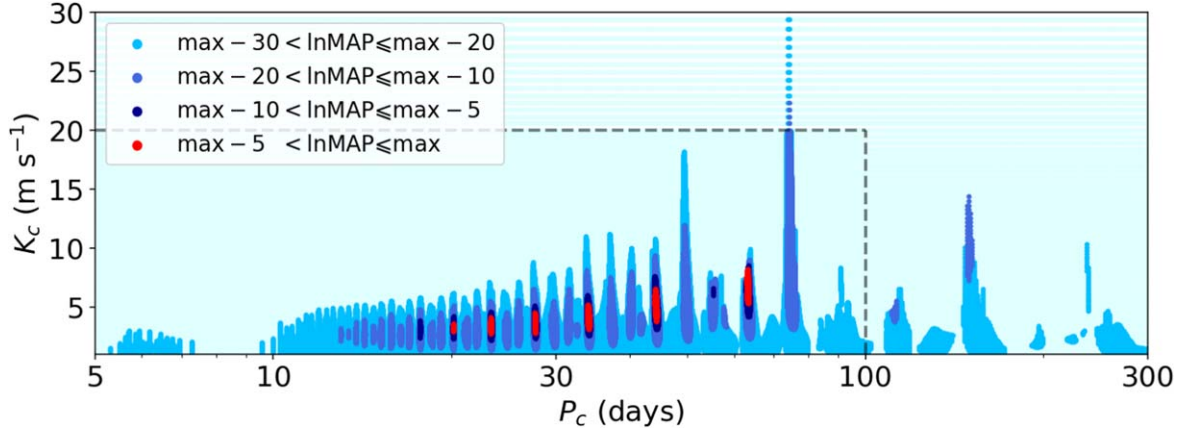
Figure 9. The ln(MAP) values of an MAP grid search in the (P_c, K_c) space using `RadVel`. Grids placed in a log-uniform distribution were applied along the P_c and K_c axes. The region framed by the gray dashed lines was also mapped with another uniformly distributed grid with a smaller interval. As informed in the upper-left legend, different ranges of the ln(MAP) values are marked by different colors. We treat the periods whose ln(MAP) values differ by five from the highest ln(MAP) value to be "the most possible solutions" of the planet candidate. The cyan region is the least favored solution with ln(MAP) differences larger than 30. We also explored the K_c space between 30 and 60 m s^{-1} but did not find any plausible solutions, hence it is not plotted here.

Table 4
Comparison of the Different RV Fitting Models[a]

Model	BIC	AIC$_c$	ΔAIC$_c$	Description
1pl-circular + trend	116.07	111.15	−1.23	One-planet, circular orbit, two trends
1pl-eccentric + trend	121.70	118.36	5.98	One-planet, eccentric orbit, two trends
1pl-circular + GP	159.06	152.27	39.89	One-planet, circular orbit, GP model
2pl-circular	118.71	112.38	0	Two-planet, circular orbits for both

Note.
[a] Only PFS data were used in the fittings.

sections. We also incorporated a generic GP model to replace the linear trends in the one-planet fit, which are found to be strongly disfavored by the data.

4.2.1. Two-planet fit in `RadVel`

We performed a grid search using the MAP fit method in `RadVel`. We constructed a grid of parameters in the (P_c, K_c) space, and for each fixed set of P_c and K_c values, we performed an MAP fit using `RadVel` with P_b, $t_{0,b}$, $t_{0,c}$, the velocity zero-points, and jitters as the free parameters. The results are shown in Figure 9, where we color coded the MAP values for each MAP fit using a set of (P_c, K_c) in the grid. We detail our choices for the priors and the (P_c, K_c) grid in the next two paragraphs. The most likely solutions of (P_c, K_c) are marked in red in Figure 9, corresponding to an ln(MAP) difference within 5 (roughly ΔAIC$_c \leqslant 10$) compared to the highest one.

The prior distributions for the free parameters are summarized in Table 5. We gave normal distributions for P_b and $t_{0,b}$ centered at the best-fit values from the photometric analysis with widths set to one order of magnitude larger than the corresponding error bars reported by the photometry. For the planet candidate, we assumed a circular orbit, and we estimated an initial guess for $t_{0,c} \sim$ BJD 2458920 by examining the residual RVs in the one-planet fit and estimating the RV zero-crossing going from redshift to blueshift (see Appendix and Figure 16).

For the (P_c, K_c) grid, we first mapped out a wider range of (5, 1) (in days and m s^{-1}, respectively) to (2000, 200) and

Table 5
Priors for the Two-planet Fit MAP Grid Search Using `RadVel`

Parameter	Prior	Description
P_b (day)	$\mathcal{N}(2.7970364, 0.00001^2)$	Orbital period of TOI-784 b
$t_{0,b}$ (BJD)	$\mathcal{N}(2459336.61220, 0.001^2)$	Time-of-transit center for TOI-784 b
$\sqrt{e_b}\sin\omega_b$	Fixed to 0	
$\sqrt{e_b}\cos\omega_b$	Fixed to 0	
K_b (m s^{-1})	$\mathcal{U}(-20.0, 20.0)$	RV semiamplitude of TOI-784 b
P_c (day)	Fixed	Orbital period of the planet candidate
$t_{0,c}$ (BJD)	$\mathcal{U}(2457000.0, 3457000.0)$	Time-of-transit center for the planet candidate
$\sqrt{e_c}\sin\omega_c$	Fixed to 0	
$\sqrt{e_c}\cos\omega_c$	Fixed to 0	
K_c (m s^{-1})	Fixed	RV semiamplitude of the planet candidate
$\dot\gamma$	Fixed to 0	Linear trend term in the RV fit
$\ddot\gamma$	Fixed to 0	Curvature term in the RV fit
μ_{PFS}	$\mathcal{N}(0.0, 10.0^2)$	Velocity zero-point for PFS
μ_{NRES1}	$\mathcal{N}(15100.0, 100.0^2)$	Velocity zero-point for NRES1
μ_{NRES2}	$\mathcal{N}(14800.0, 100.0^2)$	Velocity zero-point for NRES2
μ_{CHRION}	$\mathcal{N}(15700.0, 100.0^2)$	Velocity zero-point for CHRION
σ_{PFS}	$\mathcal{U}(0.0, 15.0)$	Jitter term for PFS
σ_{NRES1}	$\mathcal{U}(0.0, 60.0)$	Jitter term for NRES1
σ_{NRES2}	$\mathcal{U}(0.0, 60.0)$	Jitter term for NRES2
σ_{CHRION}	$\mathcal{U}(0.0, 60.0)$	Jitter term for CHRION

Table 6
Priors and Best-fit Values of the Two-planet Fit Using `Juliet`

Parameter	Prior	Best-fit	Description
P_b (day)	$\mathcal{N}(2.7970409, 0.00001^2)$	$2.7970343^{+0.0000063}_{-0.0000063}$	Orbital period of TOI-784 b
$t_{0,b}$ (BJD)	$\mathcal{N}(2459336.61220, 0.001^2)$	$2459336.61221^{+0.00059}_{-0.00073}$	Time-of-transit center for TOI-784 b
$\sqrt{e_b}\,\sin\omega_b$	Fixed	0	
$\sqrt{e_b}\,\cos\omega_b$	Fixed	0	
K_b (m s^{-1})	$\mathcal{U}(-20.0, 20.0)$	$4.67^{+0.20}_{-0.19}$	RV semiamplitude of TOI-784 b
P_c (day)	$\mathcal{U}(10.0, 450.0)$	$44.30^{+0.07}_{-0.06}$	Orbital period of the planet candidate
$t_{0,c}$ (BJD)	$\mathcal{U}(2457000.0, 3457000.0)$	$3079945^{+210953}_{-273077}$	Time-of-transit center for the planet candidate
$\sqrt{e_c}\,\sin\omega_c$	Fixed	0	
$\sqrt{e_c}\,\cos\omega_c$	Fixed	0	
K_c (m s^{-1})	$\mathcal{U}(0.0, 60.0)$	$4.64^{+0.34}_{-0.41}$	RV semiamplitude of the planet candidate
$\mu_{\rm PFS}$	$\mathcal{N}(0.0, 10.0^2)$	$0.04^{+0.36}_{-0.40}$	Velocity zero-point for PFS
$\sigma_{\rm PFS}$	$\mathcal{U}(0.0, 15.0)$	$0.87^{+0.20}_{+0.17}$	Jitter term for PFS

found no plausible solutions beyond $\sim$60 m s^{-1} and 300 days. We thus narrowed down the grid to a range of (5, 1) to (300, 60) (days, m s^{-1}). In order to perform a smoother and more careful search around the left corner region of the (P_c, K_c) space where a larger MAP value appears (red dots in Figure 9), we divided the parameter space into log-uniform grids with 600 and 150 points along the P_c and K_c axes, respectively. We also created a more concentrated uniformly distributed grid with 0.05 m s^{-1} and 0.1 day intervals for the region of (5, 1) to (100, 20) (gray dashed lines framed in Figure 9) to verify that varying the density of the grid will not result in additional islands of the possible solutions.[31]

In summary, the six most likely values of P_c have been revealed: $\sim$20, 23, 28, 34, 44, and 63 days.[32] The MAP value of the 63 day solution is more sensitive to the chosen grid, i.e., the inputted (P_c, K_c) values compared to others, which illuminates that it should be a less stable or shallower local minimum (see also Section 4.2.2). We list the six (P_c, K_c) combinations with the highest MAP values in each group along with the derived $M_c \sin i_c$ and the corresponding ln(MAP) values in Table 7. K_b has an average of 4.7 m s^{-1} over the most possible solutions in the red islands of Figure 9, which is consistent with the one-planet fit we discussed in Appendix within the 1σ level. This consistency demonstrates that the constraint on planet b's mass is insensitive to the orbital solution of the planet candidate.

4.2.2. Two-planet fit in `Juliet`

We also performed a two-planet fit using `Juliet` with the same priors as in our `RadVel` grid search, except for K_c and P_c, where we adopted uniform priors of $\mathcal{U}(0, 60)$ and $\mathcal{U}(10.0, 450.0)$ (see Table 6). Figure 10 shows a corner plot of the marginalized posterior distributions of K_b, P_b, K_c, and P_c (a complete version with all variables included is shown in Figure 21). The lower panel of Figure 10 is an enlarged plot of the P_c–K_c posterior space along with the corresponding

histogram for each parameter. There are six peaks in the posterior distribution of P_c, which are at values consistent with those we obtained from the six groups in the `RadVel` MAP grid search (Section 4.2.1).

We should note that the relative height of each possible P_c in the histogram, i.e., the number of points in each island in the posterior space (orange circles in Figure 10, hereafter posterior samples) do not reflect the relative probability for each solution. The fraction of posterior samples for each possible P_c varies between runs even if we set the same priors and same settings for the nested sampling (including the number of live points $n_{\rm live}$[33]). We checked the results for runs with 500, 1000, 2000, 3000, 4000, 5000, and 6000 live points and found that in general, more posterior samples were mapped out around each possible (P_c, K_c) pair with an increasing number of live points. The five islands of the (P_c, K_c) pair from 20 to 44 days emerge significantly more clearly in the marginalized posterior distributions after $n_{\rm live}$ was increased to 1000, while the posterior samples around the 63 day solution only appeared when $n_{\rm live} = 5000$, which may imply that this solution is rather unstable or has a narrower or shallower local minimum in the posterior space. Since we also found the 63 day solution in the MAP grid search using `RadVel`, we adopted $n_{\rm live} = 5000$ and present the results in Figure 10.

Though the relative probabilities of these six posterior peaks are unreliable (e.g., Salomone et al. 2018), the distribution within each local minimum should be trustworthy. We thus did a more concentrated search in the posterior space around each solution with `Juliet` to estimate the uncertainties of P_c and K_c of the six possible solutions. To be specific, for each of the six solutions, we set a uniform prior for P_c around each solution with a width wide enough to cover this local minimum fully and was away from other nearby local minima. We also verified that varying the choice of the prior width did not affect the final posterior for each local minimum as long as the width is wide enough (e.g., one order of magnitude larger than the posterior range). The six possible solutions for the planet candidate and their estimated uncertainties from the individual posterior distributions are reported in Table 7. Phase-folded

---

[31] We would get more (P_c, K_c) pairs falling into the red regions in Figure 9, naturally, if we choose a higher resolution for the grid, but the results should not differ in any significant way with the current grid. It is also unlikely that there would be new islands of (P_c, K_c) pairs with high MAP values, since our MAP results using `RadVel` are consistent with the posterior space we mapped out using `Juliet` in the following subsection.

[32] The same analysis was performed using joint RVs from PFS, NRES, and CHIRON for completeness, in which we found the same six best sets of P_c and K_c as expected.

[33] We applied the nested sampling implemented via `PyMultiNest` based on the MultiNest algorithm as described in Section 4.1.1. A live point stands for a series of test points uniformly distributed within the given prior for each variable parameter at the beginning, and they are then kept or rejected according to their likelihood (see, e.g., Feroz et al. 2009 for a detailed description).
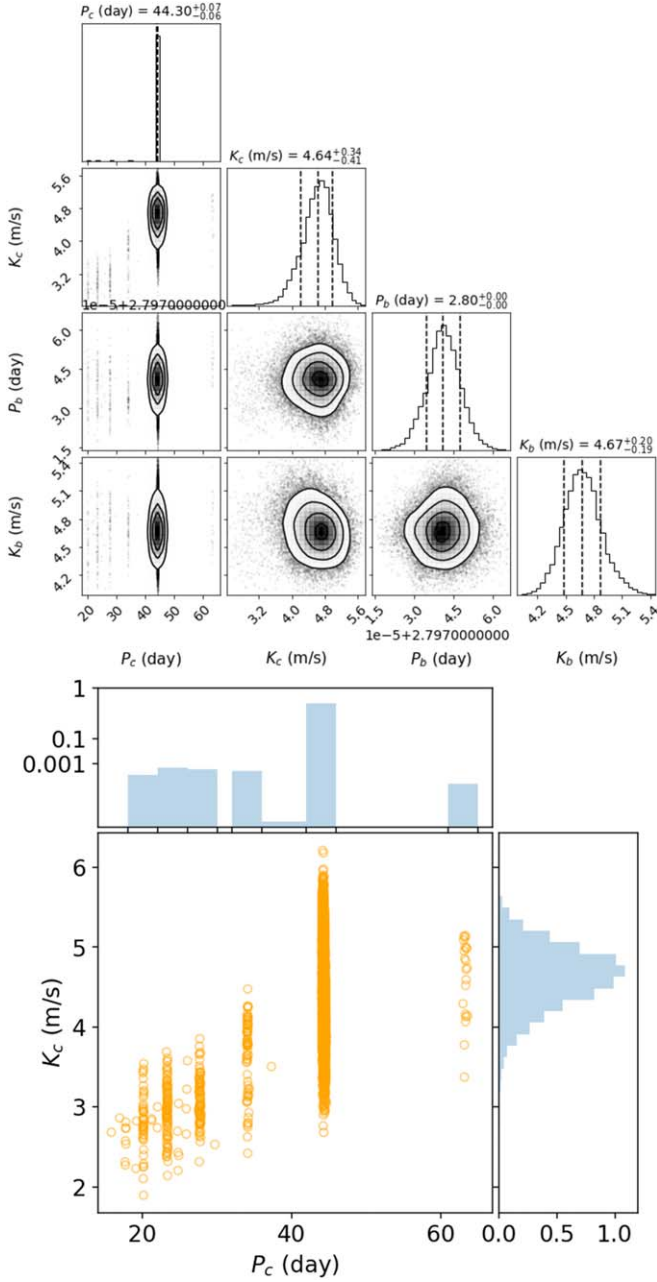
Figure 10. Top: corner plot of the posteriors of partial variable parameters in the two-planet fit using `Juliet` at $n_{\rm live} = 5000$. Bottom: an enlarged version of the P_c–K_c posterior space. The histogram of P_c is plotted on a log scale.

Table 7
Possible Solutions of TOI-784 c Found with `RadVel` and `Juliet`

K_c (m s^{-1})	P_c (day)	a_c (au)	$M_c \sin i_c$ ($M_\oplus$)	ln(MAP) values
		RadVel		
3.20	20.15	0.14	12.79	−59.45
3.40	23.30	0.15	14.26	−56.53
3.60	27.70	0.17	16.00	−55.59
4.10	34.05	0.20	19.51	−55.52
5.06	44.25	0.24	26.28	−56.21
7.00	63.20	0.30	40.95	−57.23
		Juliet		
$3.16^{+0.24}_{-0.24}$	$20.128^{+0.017}_{-0.018}$	$0.14^{+0.00}_{-0.01}$	$12.6^{+1.4}_{-1.3}$	⋯
$3.31^{+0.23}_{-0.24}$	$23.310^{+0.023}_{-0.022}$	$0.15^{+0.01}_{-0.01}$	$13.8^{+1.4}_{-1.4}$	⋯
$3.51^{+0.25}_{-0.26}$	$27.682^{+0.033}_{-0.030}$	$0.17^{+0.01}_{-0.01}$	$15.5^{+1.6}_{-1.6}$	⋯
$3.98^{+0.26}_{-0.28}$	$34.065^{+0.045}_{-0.042}$	$0.20^{+0.01}_{-0.01}$	$18.9^{+2.0}_{-1.9}$	⋯
$4.68^{+0.38}_{-0.40}$	$44.296^{+0.069}_{-0.065}$	$0.24^{+0.01}_{-0.01}$	$24.2^{+2.8}_{-2.7}$	⋯
$5.35^{+0.43}_{-0.56}$	$63.393^{+0.135}_{-0.110}$	$0.30^{+0.01}_{-0.01}$	$31.1^{+3.6}_{-3.9}$	⋯

We compare the two-planet fit with other model settings in Table 4. As discussed in the preceding sections, the planet candidate has multiple orbital solutions. We report the BIC and AIC$_c$ values of the model with the highest MAP value, where P_c and K_c were fixed at 34.05 days and 4.1 m s^{-1}, respectively (see Table 7). While the model of the one-planet fit with the circular orbit assumption plus trends has a lower AIC$_c$ than the two-planet fit, we cannot consider it the most favored model, since the combination of two linear trends is artificially included and unphysical.

4.3. Does Planet Candidate c Transit?

Based on the possible (P_c, K_c) provided in Section 4.2, we derived the corresponding $M_c \sin i_c$ values and then estimated the corresponding radius, R_c values, based on an empirical M–R relation with the python package `MRExo` (Corrales 2015). We estimated the transit depths and durations using Equation (3) in Seager (2002). Overall, the transit depth is typically larger than 900 ppm and the duration can last for at least 4.8 hours.

Comparing the derived transit depths and durations with those of TOI-784 b, whose depth and duration are roughly 400 ppm and 2.4 hours, respectively, there should be an evident signal in the TESS photometry assuming planet candidate c transits and has the best-fit parameters we found in the two-planet RV fits (Section 4.2). In order to quantify the null detection of planet c's transit, we performed an injection-and-recovery test based on the algorithm used in Gan et al. (2023). We injected a series of transit signals into the detrended TESS light curve with various sets of values for the period P_i and radius R_i of the planet candidate. We chose the ranges of P_i and R_i to cover the possible solutions we described in Section 4.2 with $P_i = [18, 66]$ days and $R_i = [2.8, 6.4]\ R_\oplus$. We divided the parameter space of P_i and R_i into a 21 by 21 grid, with each bin covering a ΔP_i of 2.4 days and ΔR_i of 0.18 $R_\oplus$. In each bin, we generated 100 sets of random P_i and R_i values with random orbital phases to create the synthetic transit signals and inject them into the detrended TESS light curve of TOI-784. We then searched for any periodic signal between 15 and 70 days with a 0.01 day grid using the box least squares (BLS) method (Kovács et al. 2002). This criterion
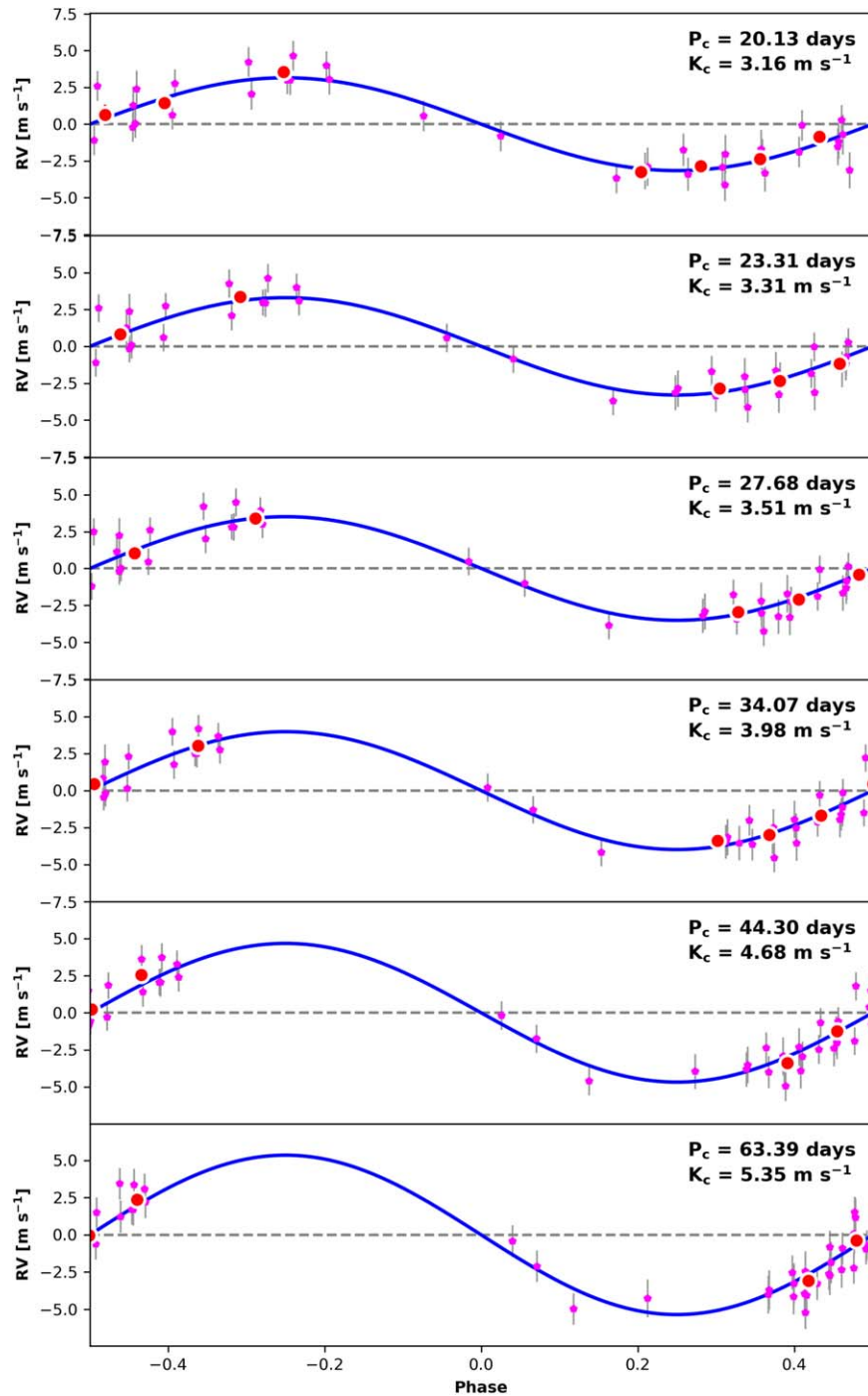
plots of the planet candidate are shown in Figure 11, with each subpanel showing the results of an MAP fit using (P_c, K_c) fixed at each possible solution as listed in Table 7.

The orbital solution for planet b is also presented in Figure 10. We derived the posterior distributions for M_b and a_b from the orbital parameters of planet b and the stellar parameters of TOI-784, which resulted in a median $M_b \sin i_b$ of 9.67 $M_\oplus$ and a_b of 0.04 au. These values are also consistent with what we found in the one-planet fit (Appendix) within 1σ. Considering i_b derived from the transit fit, which is $88.60^{\circ+0.84}_{-0.86}$, we calculated the mass for planet b M_b to be $9.67^{+0.83}_{-0.82}\ M_\oplus$.

We present the properties of planet b and the planet candidate obtained from both the photometric (Section 4.1) and RV analyses (Section 4.2) in Table 8.

Figure 11. Phase-folded RV plots of the planet candidate with the most probable six periods from the two-planet fit in `Juliet`. We assumed a circular orbit for the planet candidate in all cases. PFS RVs are shown in magenta, with the big red dots representing the binned data points.

is feasible because we can successfully find TOI-784 b whose depth and duration are much smaller using the same criterion. We define an injected synthetic planet as "recovered" when the period with the highest S/N reported by the BLS search is within 0.05% from the injected period and its harmonics (1/2 or integers) are with S/N > 10.

Due to the longer period of the planet candidate and the relatively short baseline of the TESS coverage separated by a two ear gap (two sectors spanning 55 days in 2019, and another two sectors in 2021), the detection completeness is sensitive to the total number of transits within the TESS coverage, as

shown in Figure 12. The typical number of transits N_t for each P_i bin is estimated by taking the average of the numbers of transits in the corresponding simulated transit injections.

We also performed injection-and-recovery tests for each possible period (yellow lines in Figure 12), incorporating the phase information of $t_{0,c}$ from the RV data, using the same strategy as described above. The injected periods P_i were randomly picked out with a corresponding K_i from the marginalized P_c-K_c posterior distribution we obtained from `Juliet` (Section 4.2.2). We then estimated the corresponding time-of-transit center $t_{0,i}$ for the selected (P_c, K_c) pair using the
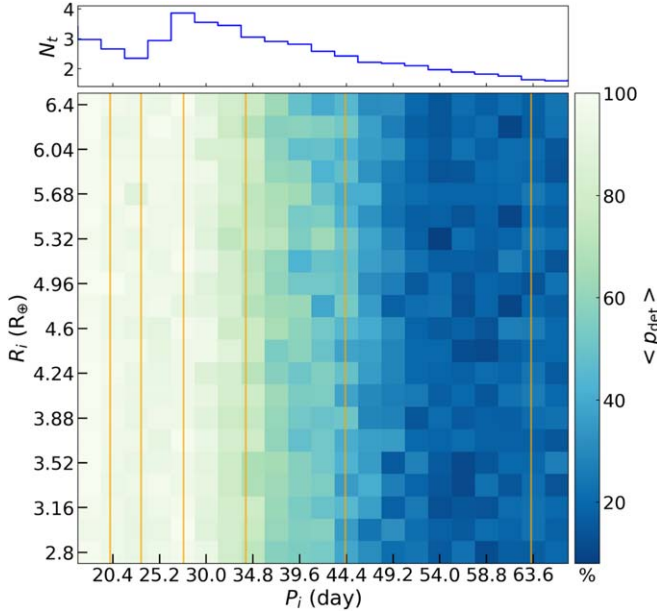
Figure 12. The result of the transit injection-and-recovery test for the planet candidate. Blue to light green represents an increasing detection possibility of its transit signal (assuming it transits). The solid blue histogram in the top panel illustrates the average number of transits within the TESS time baseline. The foreground yellow solid lines mark the six possible orbital solutions of the planet candidate found in `Juliet`.

Table 8
Composite Parameters for Planet b and Planet Candidate c from the
Photometric and RV Analyses

Parameter	Value
Planet b	
$t_{0,b}$ (BJD − 2457000)	$2336.61221^{+0.00044}_{-0.00050}$
P_b (day)	$2.7970365^{+0.0000031}_{-0.0000030}$
K_b (m s^{-1})	$4.67^{+0.20}_{-0.19}$
e_b	Fixed to 0
a_b (au)	$0.038^{+0.001}_{-0.001}$
M_b ($M_\oplus$)	$9.67^{+0.83}_{-0.82}$
R_b ($R_\oplus$)	$1.93^{+0.11}_{-0.09}$
i_b (°)	$88.60^{+0.84}_{-0.86}$
ρ_b (g/cm^3)	$7.4^{+1.4}_{-1.2}$
The planet candidate	
P_c (day)	20, 23, 28, 34, 44, 63
K_c (m s^{-1})	3.2–5.4 from `Juliet`
e_c	Fixed to 0
a_c (au)	0.14–0.30
$M_c \sin i_c$ ($M_\oplus$)	12.6–31.1
i_c (°)	⩽ 88.3 − 89.2

MAP fit in `RadVel` to include the phase information. The radius of the synthetic planet R_i was given by a uniform distribution ranging from 2 to 7 R$_\oplus$. The results of the transit detection possibility as a function of the planet size are shown in Figure 13, which resembles the general trends in Figure 12. The average detection completeness integrated over the whole radius range is 99.9%, 90.4%, 98.9%, 97.8%, 15.0%, and 19.5% for the six possible periods from 20 to 63 days, respectively.

Therefore, the fact that TESS did not report a transit detection of planet candidate c suggests that it either does not
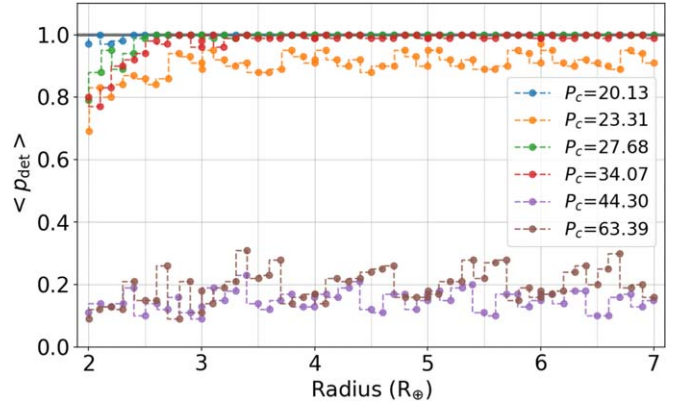
Figure 13. Detection probability as a function of the planet radius. Different colors correspond to the six possible periods of the planet candidate estimated from `Juliet`, as shown in the legend. The results here incorporate the phase information from the RV data, and thus they are different from Figure 12, which used a random phase.

transit (if having a relatively shorter period) or its transits escaped TESS's detection due to its long period (if $P_c > \sim 40$ days). TESS reobserved TOI-784 in Sectors 63–64 in 2023 March–May, and these additional TESS data would provide more leverage to constrain the transit of this planet candidate.

Assuming that the planet candidate does not transit, we can estimate the possible range of its orbital inclination. Our two-planet analysis provided a group of possible values of the semimajor axis a_c for the planet candidate, with the minimum and maximum values being 0.14 and 0.30 au, respectively. These translate to an orbital inclination of $i_c \leqslant 88°.3$ or $89°.2$, respectively. Compared with the inclination of TOI-784 b estimated from the TESS light curve, $88.60°^{+0.84}_{-0.86}$, these two planets could be possibly coplanar even if the second planet does not transit.

5. Discussion and Conclusions

Properties of planet b and planet candidate c are summarized in Table 8. In Figure 14, we show the M–R diagram for the sample of confirmed exoplanets (data from TEPCAT database; Southworth 2011) with TOI-784 b marked in red.[34] The solid and dashed lines illustrate theoretical models with different compositions according to Zeng et al. (2016), among which Earth composition is estimated with 34% Fe + 66% MgSiO$_3$. The M–R relation illuminates that TOI-784 b could have a rocky core and presumably no H/He gas envelope. The estimated density of TOI-784 b using our measured radius and mass is $7.4^{+1.4}_{-1.2}$ g cm^{-3}, which also suggests that TOI-784 b is a super-Earth consistent with a rocky composition and perhaps no significant atmosphere or ocean. We computed the transmission spectroscopy metric (TSM) and emission spectroscopy metric (ESM) for planet b using Equations (1) and (4) from Kempton et al. (2018). The TSM and ESM values obtained were 36.2 and 6.8, respectively. These values fall below the threshold recommended by Kempton et al. (2018) for high-quality atmospheric characterization targets for a planet with a radius of 1.5–10, R$_\oplus$, and thus may not suitable for James Webb Space Telescope (JWST) to observe. However,

---

[34] The plot was created using the `fancy-mass--radius-plot` package at https://github.com/oscaribv/fancy-mass--radius-plot by Barragán et al. (2018).
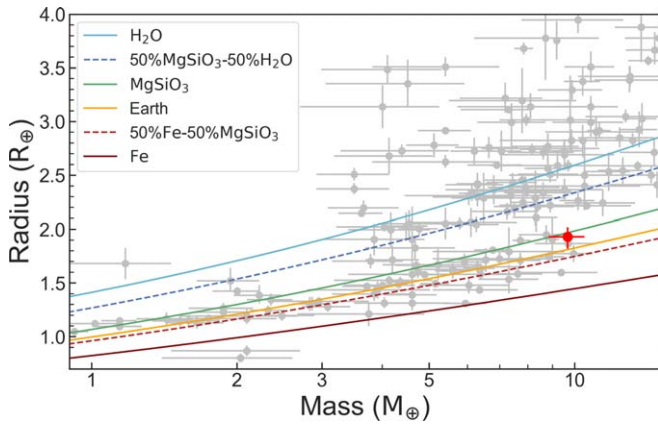
Figure 14. The M–R relation. The background gray dots are planets from the TEPCAT database. Solid and dashed curves indicate different planet compositions. TOI-784 b (the red point) is between the green and orange lines representing a $MgSiO_3$ core and Earth composition, respectively, which implies that TOI-784 b is a rocky planet, i.e., the same conclusion found in our analyses. Considering the uncertainty of the planet size, TOI-784 b could be pure rocky or have a small amount of atmosphere consisting of heavy elements (e.g., H_2O, CO_2, etc.).

Figure 15. Relation of planet insolation flux and radius. Forward blue points are exoplanets with data taken from the NASA exoplanet archive and background contours indicate their number density. The dashed line illustrates theoretical predictions under gas-poor formation scenarios (Lopez & Rice 2018), while the black dotted line is derived by Martinez et al. (2019) using the CKS sample with the shaded green region representing the 1σ error.

planet b may have a small amount of volatiles with heavy molecules such as H_2O or CO_2 instead of H/He given its small size, which is not surprising given its short period and relatively strong stellar irradiation.

We also compared TOI-784 b with other super-Earths or sub-Neptunes using data from the NASA Exoplanet Archive.[35] Figure 15 shows the insolation flux S_{pl} versus planet radius R_{pl} of TOI-784 b in comparison with other known transiting planets. The background contour represents the observed planet number density (not occurrence rate). The dotted line with the 1σ error bar shaded in light green is the empirical relation for the radius valley derived by Martinez et al. (2019), which is consistent with both photoevaporation and core-powered mass-loss models of planet formation. The dashed black line represents the radius valley in a gas-poor formation scenario as predicted by Lopez & Rice (2018).

TOI-784 b has a radius of $1.9^{+0.11}_{-0.09}R_\oplus$, which is at the upper edge of the radius valley (Fulton et al. 2017; Fulton & Petigura 2018). Various scenarios as mentioned above were proposed to explain this valley. A planet will receive UV/X-ray flux from its parent star, which will erode its gas envelope (photoevaporation). As a consequence, planets on a closer orbit to their hosts experience stronger irradiation and become naked rocky cores, while outer planets tend to keep their envelopes and have a transit radius roughly twice the size of the rocky core (Owen & Wu 2017). Core-powered mass loss, considering the effect of the cooling core, can also strip envelopes and cause a lack of planets with intermediate radii (Ginzburg et al. 2018; Gupta & Schlichting 2020). Photoevaporation, as well as the core-powered mass-loss scenario, predicts a positive correlation in the insolation flux versus planet size plane, while gas-poor formation makes the opposite prediction (see Table 2 and Figure 11 in Cloutier & Menou 2020 for a summary) as shown in Figure 15. TOI-784 b is located at the lower edge of the radius valley (in the R_p-S_p plane) predicted by photoevaporation or core-powered mass loss, which is

consistent with the atmospheric loss formation scenario considering its rocky composition.

Moreover, the well-separated planet candidate and TOI-784 b (period ratio > 7) may result from a violent mass-loss history (Wang & Lin 2023). According to previous works on the stability of multiplanet systems with mass-loss processes, it is possible to keep the system in a stable configuration if the inner planet loses less than 5%–10% of its total mass over a timescale larger than 2×10^4 yr (Matsumoto & Ogihara 2020; Wang & Lin 2023). After such "gentle" mass-loss process, a closely packed system could still remain stable. On the other hand, if the inner super-Earth experiences violent atmosphere mass loss over a shorter timescale, in which about 20%–30% of its total mass is lost, a widely separated configuration may form as a consequence of violent dynamical interactions, including collisions and mergers between planets. Therefore, the well-separated configuration of the TOI-784 system is consistent with the possibility that the inner planet once held a considerably amount of atmosphere.

In addition to the mass-loss formation scenario for TOI-784 b, there is another possibility that this rocky planet could be a failed core and preserved as a super-Earth in the natal disk (e.g., Ida & Lin 2004). According to Chen et al. (2020), even though a massive core reaches the pebble-isolation mass (a few to $10 M_\oplus$) before the severe depletion of the gas disk (which is different from formation in a gas-poor environment), an increasing grain opacity in the planetary envelope could significantly suppress the runaway gas accretion given its stellar proximity.

In summary, we confirmed a TESS-discovered transiting super-Earth, TOI-784 b, and identified an additional planet candidate in the system using RVs taken by Magellan/PFS, CHIRON, and LCOGT/NRES. TOI-784 b is a $1.93 R_\oplus$ super-Earth, with a period of 2.80 days and a mass of $9.67 M_\oplus$. The bulk density of TOI-784 b indicates that its composition is likely rocky, with a minimum amount of volatiles, which is consistent with the prediction of the photoevaporation or core-powered mass-loss scenarios. We also found a planet candidate revealed by the RV follow-up observations, but unfortunately,

---

[35] https://exoplanetarchive.ipac.caltech.edu, accessed 2022 June 21.

our observed RVs did not map out its entire orbit. We performed a grid search in parameter space using `RadVel` as well as a two-planet fit using `Juliet` to investigate possible solutions for the planet candidate (Section 4.2). Six possible orbital solutions for the candidate have been found, with the period ranging from 20 to 63 days and mass being 12–31 $M_\oplus$. Given its large minimum mass, the candidate is likely a Neptune-mass planet rich in volatiles, unlike TOI-784 b. We performed an injection-and-recovery test to characterize the likelihood of the planet candidate actually transiting but being missed by TESS, and we conclude that it is more likely to be an intrinsically nontransiting planet, although we cannot rule out the transit scenario completely, especially if it has a period around or longer than 40 days.

The TOI-784 system contains a transiting small planet in the inner orbit and an outer, likely warm, planet candidate that probably does not transit, which can contribute to the statistical sample of multiplanet systems with mass measurements. The determination of the outer planet candidate's properties requires future observations, especially more TESS observations in the Extended Mission and more RV follow up.

Appendix
One-planet fit

Due to a lack of RV data, as we cannot fully constrain the orbit of the additional planet candidate (which we called "planet c" for simplicity in the paper), planet b's solution would be dependent on the choice of the specific two-planet fit. In this appendix, we explore the robustness of planet b's parameters and check if we could constrain the mass of planet b regardless of the choice for the orbital solution of the planet candidate.

Before we obtained the four more data points in 2022 from PFS, the PFS data had unfortunately only captured the same rising phase of the second planet separated by a year, which makes it challenging for the RV analysis due to degeneracy in the period and RV amplitude parameter space for the second object. Therefore, we first constructed a composite model with a linear trend for each of the first two sections of PFS data plus a Keplerian model for planet b, which would be a more generic model describing the signals from the second object more commonly used in the RV fit for systems with long-period massive companions (e.g., Crepp et al. 2012; Montet et al. 2014). Here we present the result of our fit to the pre-2022 PFS RVs using this simple model that consists of one Keplerian model plus two trends. An alternative model including both a linear trend and curvature has also been tested, but model comparison with BIC and AIC_c indicates that this was not the favored model.

The best-fit Keplerian+2 trends model is shown in Figure 16. Similar to Section 4.2.1, we used `RadVel` (Fulton et al. 2018) to perform this fit, where an MAP optimization will first be run in a fit via `scipy.optimize.minimize`, followed by an MCMC analysis via `emcee` (Foreman-Mackey et al. 2013) to estimate the uncertainty for each parameter. In our case, we required the model to fit two independent linear trends, which is not supported by `RadVel`, so we modified its source code and added an additional term in the model.

Priors and best-fit values are listed in Table 9. To be specific, we gave normal distributions for the orbital period P_b and the time-of-transit center $t_{0,b}$ according to the optimized values we obtained in the previous photometric analysis (Section 4.1). The eccentricity was fixed to zero as we discussed in Section 4.1.1. The initial guess of K_b was $5\,\mathrm{m\,s^{-1}}$ and we set a uniform distribution of $\mathcal{U}(-20, 20)$ for its prior, which is roughly twice the RV range of PFS data used here. We gave two different slopes, $\dot{\gamma}_1$ and $\dot{\gamma}_2$, for the two sections of RV data
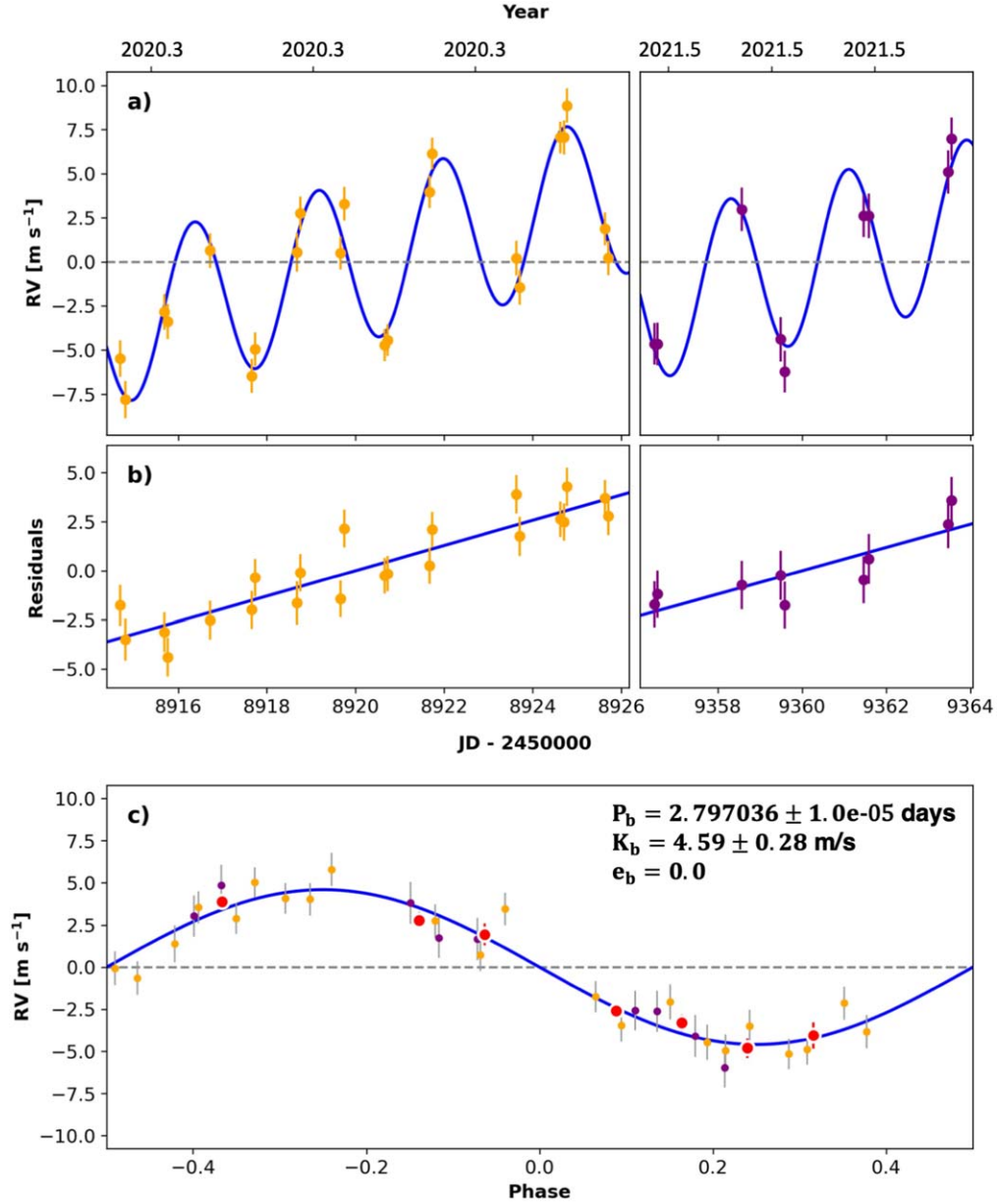
Figure 16. The one-planet RV fit with two independent trends in the model. The orange and purple dots represent the first and second year PFS data, respectively. The best-fit model is shown by the thin blue line. (b) The linear residuals after subtracting the signal from TOI-784 b. (c) The phase-folded RV plot of TOI-784 b. Red circles are the same velocities binned in 0.08 units of the orbital phase.

Table 9
Priors and Best-fit Values of the One-planet Fit

| Parameter	Prior	Best-fit	Description
P_b (day)	$\mathcal{N}(2.7970364, 0.00001^2)$	$2.797036^{+0.000010}_{-0.000010}$	Orbital period of TOI-784 b
$t_{0,b}$ (BJD)	$\mathcal{N}(2459336.61220, 0.001^2)$	$2459336.6122^{+0.0010}_{-0.0010}$	Time-of-transit center for TOI-784 b
$\sqrt{e_b}\sin\omega_b$	Fixed	0	
$\sqrt{e_b}\cos\omega_b$	Fixed	0	
K_b (m s^{-1})	$\mathcal{U}(-20.0, 20.0)$	$4.59^{+0.28}_{-0.29}$	RV semiamplitude of TOI-784 b
$\dot{\gamma}_1$	RadVel default	$0.643^{+0.067}_{-0.065}$	Linear trend term in the RV fit
$\ddot{\gamma}_1$	Fixed	0	Curvature term in the RV fit
$\dot{\gamma}_2$	RadVel default	$0.59^{+0.18}_{-0.18}$	Linear trend term in the RV fit
$\ddot{\gamma}_2$	Fixed	0	Curvature term in the RV fit
$\mu_{\mathrm{PFS},1}$	$\mathcal{N}(0.0, 10.0^2)$	$0.50^{+0.23}_{-0.23}$	Velocity zero-point for PFS
$\mu_{\mathrm{PFS},2}$	$\mathcal{N}(0.0, 10.0^2)$	$-2.12^{+0.44}_{-0.43}$	Velocity zero-point for PFS
σ_{PFS}	$\mathcal{U}(0.0, 15.0)$	$0.77^{+0.24}_{-0.23}$	Jitter term for PFS
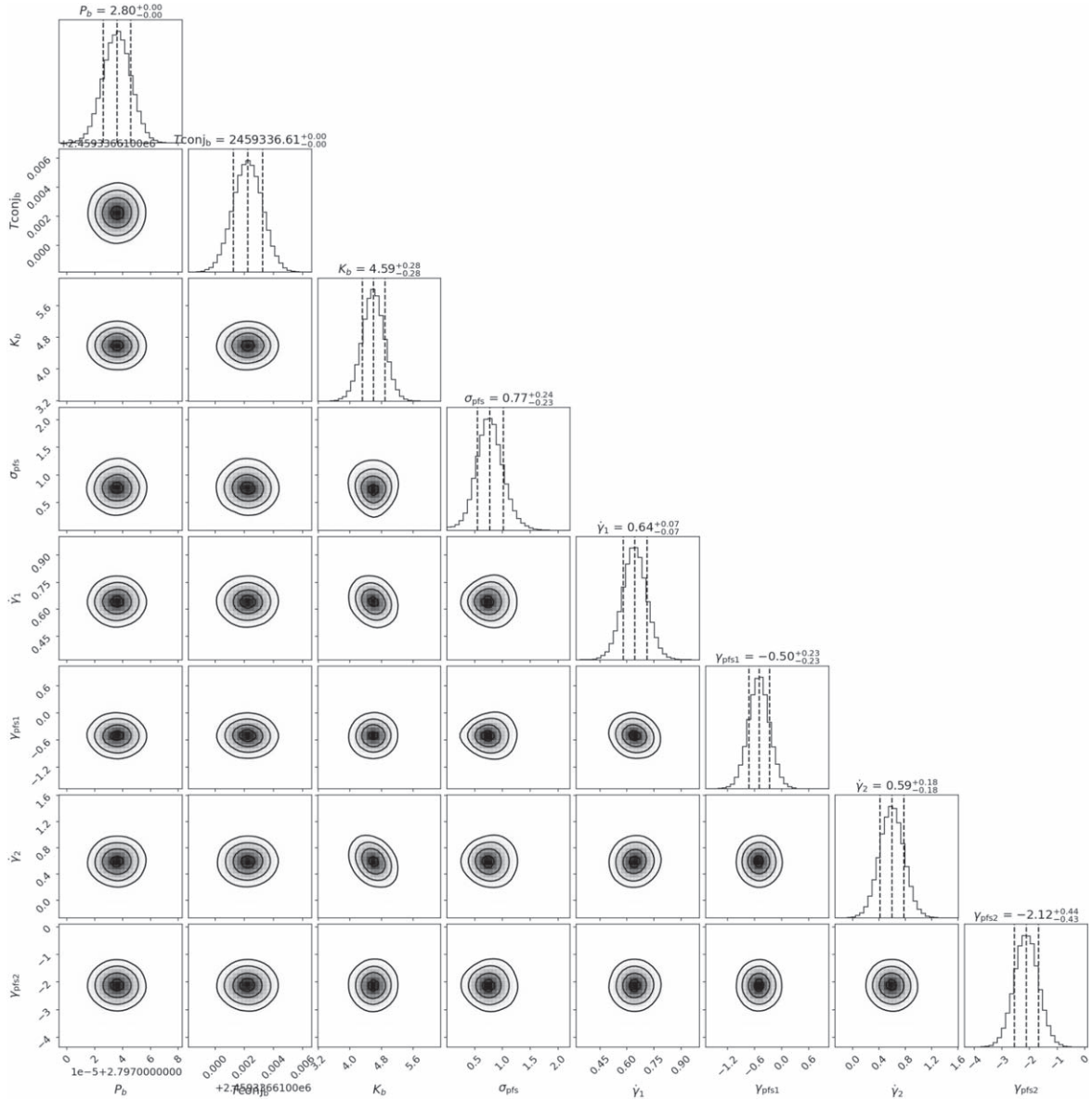
Figure 17. Corner plot of all fitted parameters in the one-planet RV fit using `RadVel`.

with initial guesses both set to zero. The two sections of data share the same jitter term σ_{PFS} but having independent offset terms, $\mu_{\mathrm{PFS,1}}$ and $\mu_{\mathrm{PFS,2}}$, of PFS, for which we gave a normal distribution $\mathcal{N}(0, 10^2)$ and two uniform distributions $\mathcal{U}(0, 15)$, respectively. The best-fit RV semiamplitude of planet b's K_b and its uncertainties are $4.59^{+0.28}_{-0.29}$ m s^{-1}, and the corresponding minimum mass is $9.47^{+0.92}_{-0.90}$ $M_\oplus$, consistent with the values we presented in the main text of this paper (Table 8). Corner plots for the marginalized posteriors of the fitted and the derived parameters are presented in Figures 17 and 18.

We then subtracted the best-fit linear trends from the RV data and performed a joint fit using `Juliet` (Espinoza et al. 2019) combining the residual RV data with the TESS light curve (Figure 19). The joint fit did not tighten the constraints on any of the parameters for planet b, and the results are consistent well within their error bars with our results presented above (Section 4).

We also performed a one-planet fit in `RadVel` including a GP model to fit the additional RV signals besides TOI-784 b. A GP model is a commonly used generic nonparametric model describing periodic or quasi-periodic signals, and is often used to describe RV jitter caused by stellar magnetic activities (e.g., Haywood et al. 2014). Here we chose to use the GP regression to model the RVs from the planet candidate as it is a flexible and generic time-series model that does not bear any astrophysical meaning, which is ideal to test the robustness of planet b's orbital solution. We used the quasi-periodic kernel implemented by `celerite` (Foreman-Mackey et al. 2017) as offered in `RadVel`. The results for our GP+planet b model are shown in Figure 20 and Table 10. The derived $M_b \sin i_b$ is $9.49^{+0.97}_{-0.94}$ $M_\oplus$, consistent with our results in Table 8 and also consistent with the results found when using the model with the two linear trends.
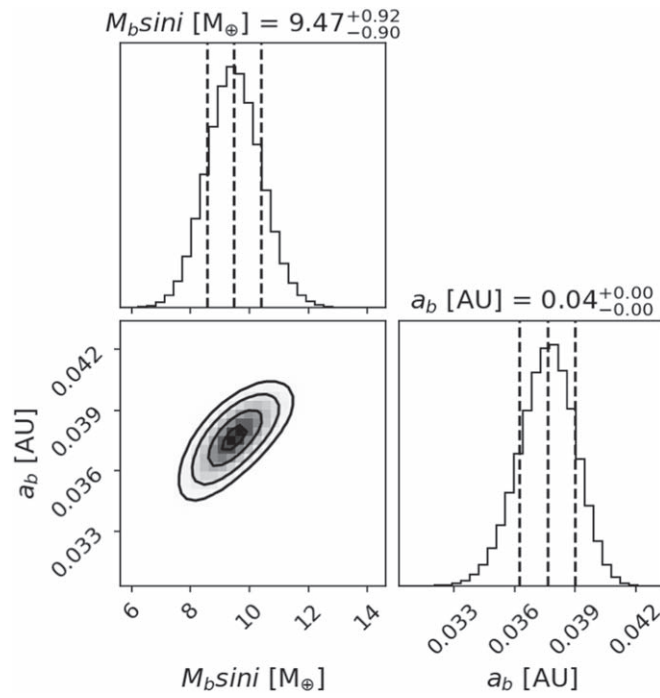
Figure 18. Corner plot of the derived parameters in the one-planet RV fit using `RadVel`.
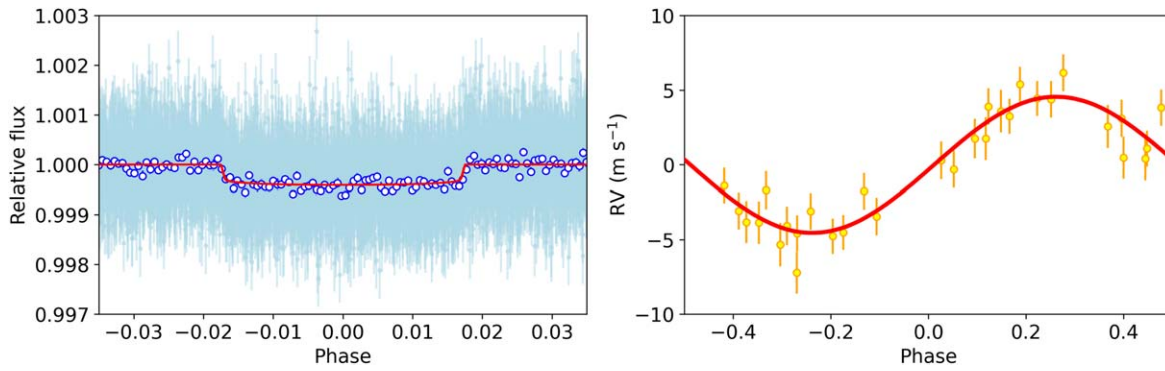

Figure 19. The joint fit of the TESS light curve and RVs of planet b using pre-2022 PFS RVs with the two best-fit linear trends subtracted. The transit fit is in the left panel, and the RV fit is on the right, with the best-fit model in red solid lines. The white dots circled by blue rings are binned TESS photometric data points with a 40 bin size.
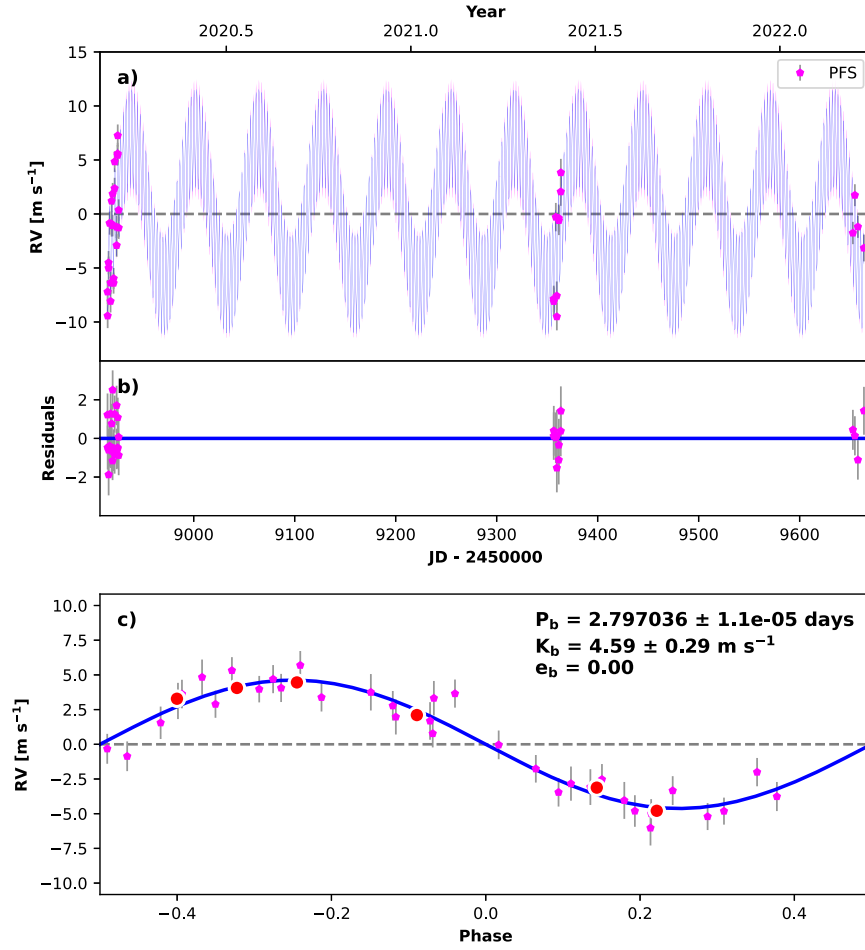
Figure 20. The one-planet RV fit with a GP model using `RadVel` and `celerite`. The magenta points are the used PFS RVs. The best-fit model is shown by the thin blue line. (b) The RV residuals after subtracting the best-fit GP and Keplerian models. (c) The phase-folded RV plot of TOI-784 b after subtracting the GP model component. Red circles are the same velocities binned in 0.08 units of orbital phase.

Table 10
Priors and Best-fit Values of the One-planet Fit Including a GP Model

| Parameter	Prior	Best-fit	Description
Planetary parameters			
P_b (day)	$\mathcal{N}(2.7970364, 0.00001^2)$	$2.797036^{+1.0e-5}_{-1.1e-5}$	Orbital period of TOI-784 b
$t_{0,b}$ (BJD)	$\mathcal{N}(2459336.61220, 0.001^2)$	$2459336.6122^{+0.0011}_{-0.0010}$	Time-of-transit center for TOI-784 b
$\sqrt{e_b}\sin\omega_b$	Fixed	0	
$\sqrt{e_b}\cos\omega_b$	Fixed	0	
K_b (m s^{-1})	$\mathcal{U}(-20.0, 20.0)$	$4.59^{+0.32}_{-0.30}$	RV semiamplitude of TOI-784 b
$\dot{\gamma}$	Fixed	0	Linear trend term in the RV fit
$\ddot{\gamma}$	Fixed	0	Curvature term in the RV fit
μ_{PFS}	$\mathcal{N}(0.0, 10.0^2)$	$-0.30^{+6.0}_{-4.8}$	Velocity zero-point for PFS
σ_{PFS}	$\mathcal{U}(0.0, 15.0)$	$0.82^{+0.25}_{-0.22}$	Jitter term for PFS
GP parameters			
B_{PFS}	$\mathcal{U}(0.0001, 10000)$	76^{+680}_{-61}	GP hyperparameter
C_{PFS}	$\mathcal{U}(0.0001, 10000)$	$0.006^{+0.23}_{-0.0057}$	GP hyperparameter
L_{PFS}	$\mathcal{U}(0.0001, 1.0e+7)$	6254^{+2600}_{-3300}	GP hyperparameter
$P_{\mathrm{rot,PFS}}$	$\mathcal{U}(10.0, 450.0)$	54^{+160}_{-27}	GP hyperparameter
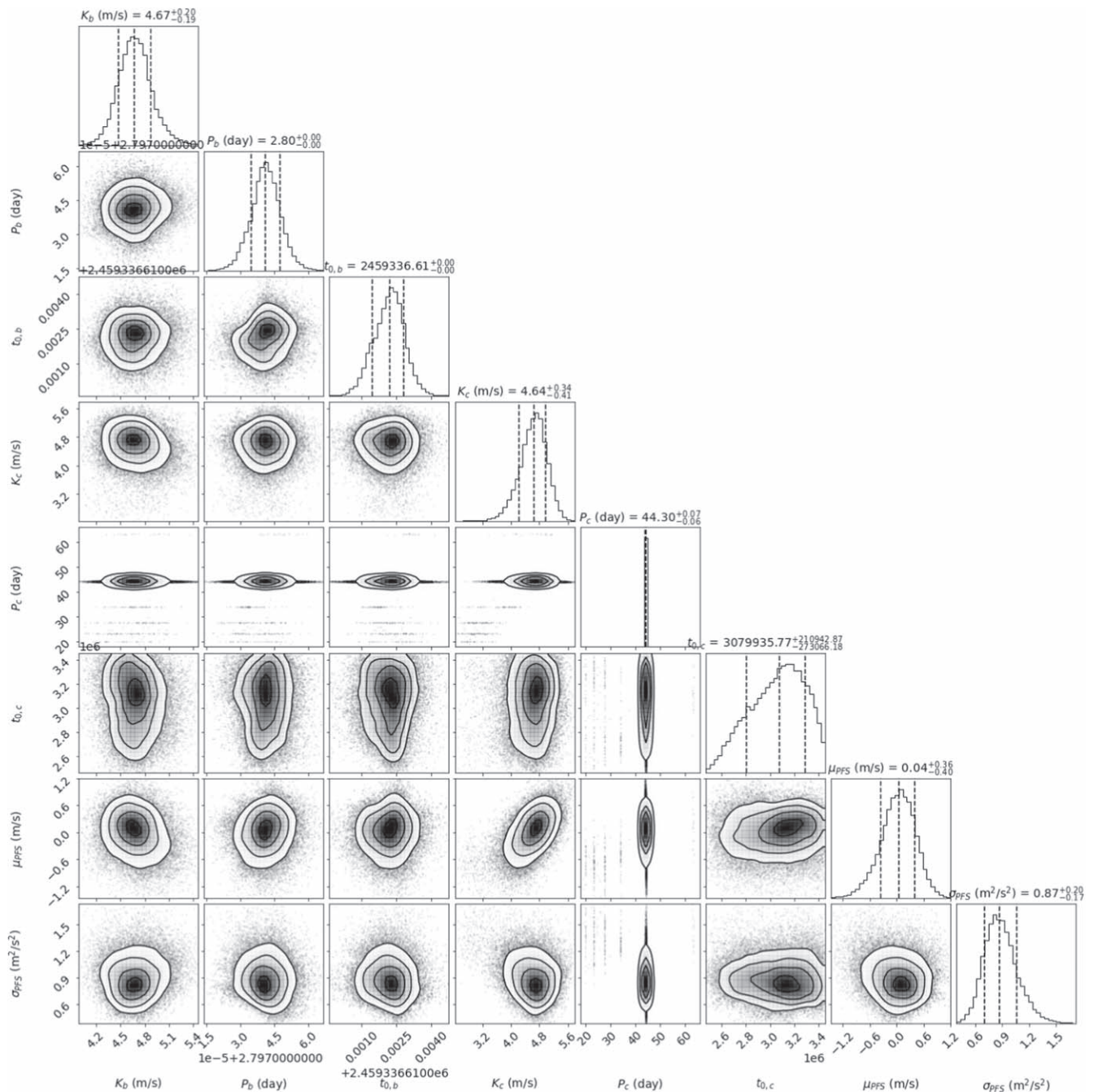
Figure 21. Corner plot of all fitted parameters in the two-planet fit using `Juliet`. See Section 4.2.2 for more details.

ORCID iDs

Xinyan Hua https://orcid.org/0000-0001-7916-4371
Sharon Xuesong Wang https://orcid.org/0000-0002-6937-9034
Tianjun Gan https://orcid.org/0000-0002-4503-9705
Avi Shporer https://orcid.org/0000-0002-1836-3120
George Zhou https://orcid.org/0000-0002-4891-3517
Keivan G. Stassun https://orcid.org/0000-0002-3481-9052
Markus Rabus https://orcid.org/0000-0003-2935-7196
Steve B. Howell https://orcid.org/0000-0002-2532-2853
Jack J. Lissauer https://orcid.org/0000-0001-6513-1659
Joshua N. Winn https://orcid.org/0000-0002-4265-047X
Jon M. Jenkins https://orcid.org/0000-0002-4715-9460
Eric B. Ting https://orcid.org/0000-0002-8219-9505
Karen A. Collins https://orcid.org/0000-0001-6588-9574

Andrew W. Mann https://orcid.org/0000-0003-3654-1602
Wei Zhu https://orcid.org/0000-0003-4027-4711
R. Paul Butler https://orcid.org/0000-0003-1305-3761
Jeffrey D. Crane https://orcid.org/0000-0002-5226-787X
Stephen A. Shectman https://orcid.org/0000-0002-8681-6136
Luke G. Bouma https://orcid.org/0000-0002-0514-5538
César Briceño https://orcid.org/0000-0001-7124-4094
Diana Dragomir https://orcid.org/0000-0003-2313-467X
William Fong https://orcid.org/0000-0003-0241-2757
Nicholas Law https://orcid.org/0000-0001-9380-6457
Samuel N. Quinn https://orcid.org/0000-0002-8964-8377
George R. Ricker https://orcid.org/0000-0003-2058-6662
Richard P. Schwarz https://orcid.org/0000-0001-8227-1020
Sara Seager https://orcid.org/0000-0002-6892-6948

Ramotholo Sefako ● https://orcid.org/0000-0003-3904-6754
Chris Stockdale ● https://orcid.org/0000-0003-2163-1437
Roland Vanderspek ● https://orcid.org/0000-0001-6763-6562

References

Astropy Collaboration, Price-Whelan, A. M., Lim, P. L., et al. 2022, ApJ, 935, 167
Astropy Collaboration, Price-Whelan, A. M., Sipőcz, B. M., et al. 2018, AJ, 156, 123
Astropy Collaboration, Robitaille, T. P., Tollerud, E. J., et al. 2013, A&A, 558, A33
Ballard, S., & Johnson, J. A. 2016, ApJ, 816, 66
Barragán, O., Gandolfi, D., Dai, F., et al. 2018, A&A, 612, A95
Batalha, N. E., Lewis, T., Fortney, J. J., et al. 2019, ApJL, 885, L25
Batalha, N. M., Rowe, J. F., Bryson, S. T., et al. 2013, ApJS, 204, 24
Behmard, A., Dai, F., & Howard, A. W. 2022, AJ, 163, 160
Borucki, W. J., Koch, D., Basri, G., et al. 2010, Sci, 327, 977
Brahm, R., Jordán, A., & Espinoza, N. 2017, PASP, 129, 034002
Brandt, T. D. 2021, ApJS, 254, 42
Brown, T. M., Baliber, N., Bianco, F. B., et al. 2013, PASP, 125, 1031
Buchhave, L. A., Latham, D. W., Johansen, A., et al. 2012, Natur, 486, 375
Buchner, J., Georgakakis, A., Nandra, K., et al. 2014, A&A, 564, A125
Burt, J., Holden, B., Wolfgang, A., & Bouma, L. G. 2018, AJ, 156, 255
Butler, R. P., Marcy, G. W., Williams, E., et al. 1996, PASP, 108, 500
Castelli, F., & Kurucz, R. L. 2003, in IAU Symp. 210, Modelling of Stellar Atmospheres, ed. N. Piskunov, W. W. Weiss, & D. F. Gray (San Francisco, CA: ASP), A20
Chen, Y.-X., Li, Y.-P., Li, H., & Lin, D. N. C. 2020, ApJ, 896, 135
Cloutier, R., & Menou, K. 2020, AJ, 159, 211
Cloutier, R., Rodriguez, J. E., Irwin, J., et al. 2020, AJ, 160, 22
Collins, K. A., Kielkopf, J. F., Stassun, K. G., & Hessman, F. V. 2017, AJ, 153, 77
Corrales, L. 2015, dust: Calculate the intensity of dust scattering halos in the X-ray, v1.0, Zenodo, doi:10.5281/zenodo.15991
Crane, J. D., Shectman, S. A., & Butler, R. P. 2006, Proc. SPIE, 6269, 626931
Crane, J. D., Shectman, S. A., Butler, R. P., et al. 2010, Proc. SPIE, 7735, 773553
Crane, J. D., Shectman, S. A., Butler, R. P., Thompson, I. B., & Burley, G. S. 2008, Proc. SPIE, 7014, 701479
Crepp, J. R., Johnson, J. A., Howard, A. W., et al. 2012, ApJ, 761, 39
Espinoza, N. 2018, RNAAS, 2, 209
Espinoza, N., Kossakowski, D., & Brahm, R. 2019, MNRAS, 490, 2262
Feroz, F., & Hobson, M. P. 2008, MNRAS, 384, 449
Feroz, F., Hobson, M. P., & Bridges, M. 2009, MNRAS, 398, 1601
Feroz, F., Hobson, M. P., Cameron, E., & Pettitt, A. N. 2019, OJAp, 2, 10
Foreman-Mackey, D., Agol, E., Ambikasaran, S., & Angus, R. 2017, AJ, 154, 220
Foreman-Mackey, D., Hogg, D. W., Lang, D., & Goodman, J. 2013, PASP, 125, 306
Fulton, B. J., & Petigura, E. A. 2018, AJ, 156, 264
Fulton, B. J., Petigura, E. A., Blunt, S., & Sinukoff, E. 2018, PASP, 130, 044504
Fulton, B. J., Petigura, E. A., Howard, A. W., et al. 2017, AJ, 154, 109
Gaia Callaboration 2018, yCat, I/345
Gaia Callaboration 2020, yCat, I/350
Gan, T., Wang, S. X., Wang, S., et al. 2023, AJ, 165, 17
Ginzburg, S., Schlichting, H. E., & Sari, R. 2018, MNRAS, 476, 759
Guerrero, N. M., Seager, S., Huang, C. X., et al. 2021, ApJS, 254, 39
Gupta, A., & Schlichting, H. E. 2020, MNRAS, 493, 792
Hamilton, D. P., & Burns, J. A. 1992, Icar, 96, 43
Hansen, B. M., & Murray, N. 2013, ApJ, 775, 53
Haywood, R. D., Collier Cameron, A., Queloz, D., et al. 2014, MNRAS, 443, 2517
He, M. Y., Ford, E. B., & Ragozzine, D. 2019, MNRAS, 490, 4575
He, M. Y., Ford, E. B., Ragozzine, D., & Carrera, D. 2020, AJ, 160, 276
Henry, T. J., Soderblom, D. R., Donahue, R. A., & Baliunas, S. L. 1996, ApJ, 111, 439
Howell, S. B., Everett, M. E., Sherry, W., Horch, E., & Ciardi, D. R. 2011, AJ, 142, 19

Ida, S., & Lin, D. N. C. 2004, ApJ, 604, 388
Jenkins, J. M. 2002, ApJ, 575, 493
Jenkins, J. M., Chandrasekaran, H., McCauliff, S. D., et al. 2010, Proc. SPIE, 7740, 77400D
Jenkins, J. M., Tenenbaum, P., Seader, S., et al. 2020, Kepler Data Processing Handbook: Transiting Planet Search, Kepler Science Document KSCI-19081-003
Jenkins, J. M., Twicken, J. D., McCauliff, S., et al. 2016, Proc. SPIE, 9913, 99133E
Jensen, E. 2013, Tapir: A web interface for transit/eclipse observability, Astrophysics Source Code Library, ascl:1306.007
Kempton, E. M., Bean, J. L., Louie, D. R., et al. 2018, PASP, 130, 1
Kovács, G., Zucker, S., & Mazeh, T. 2002, A&A, 391, 369
Kreidberg, L. 2015, PASP, 127, 1161
Kurucz, R. L. 1979, ApJS, 40, 1
Lacedelli, G., Malavolta, L., Borsato, L., et al. 2021, MNRAS, 501, 4148
Lehtinen, J., Jetsu, L., Hackman, T., Kajatkari, P., & Henry, G. W. 2016, A&A, 588, 1
Li, J., Tenenbaum, P., Twicken, J. D., et al. 2019, PASP, 131, 024506
Lissauer, J. J., Ragozzine, D., Fabrycky, D. C., et al. 2011, ApJS, 197, 8
Lopez, E. D., & Rice, K. 2018, MNRAS, 479, 5303
Lubin, J., Van Zandt, J., Holcomb, R., et al. 2022, AJ, 163, 101
Luque, R., & Pallé, E. 2022, Sci, 377, 1211
Lightkurve Collaboration, Cardoso, J. V. d. M., Hedges, C., et al. 2018, Lightkurve: Kepler and TESS time series analysis in Python, Astrophysics Source Code Library, ascl:1812.013
Mamajek, E. E., & Hillenbrand, L. A. 2008, ApJ, 687, 1264
Martinez, C. F., Cunha, K., Ghezzi, L., & Smith, V. V. 2019, ApJ, 875, 29
Matsumoto, Y., & Ogihara, M. 2020, ApJ, 893, 43
Mermilliod, J. C. 2006, yCat, II/168
Montet, B. T., Crepp, J. R., Johnson, J. A., Howard, A. W., & Marcy, G. W. 2014, ApJ, 781, 28
Mulders, G. D., Pascucci, I., Apai, D., & Ciesla, F. J. 2018, AJ, 156, 24
Owen, J. E., & Wu, Y. 2017, arXiv:1705.10810
Paredes, L. A., Henry, T. J., Quinn, S. N., et al. 2021, AJ, 162, 176
Petigura, E. A., Rogers, J. G., Isaacson, H., et al. 2022, AJ, 163, 179
Ricker, G. R., Winn, J. N., Vanderspek, R., et al. 2015, JATIS, 1, 014003
Salomone, R., South, L. F., Drovandi, C. C., & Kroese, D. P. 2018, arXiv:1805.03924
Schlegel, D. J., Finkbeiner, D. P., & Davis, M. 1998, ApJ, 500, 525
Seager, S. 2002, arXiv:0206228v1
Siverd, R. J., Brown, T. M., Barnes, S., et al. 2018, Proc. SPIE, 10702, 107026C
Smith, J. C., Stumpe, M. C., Van Cleve, J. E., et al. 2012, PASP, 124, 1000
Southworth, J. 2011, MNRAS, 417, 2166
Speagle, J. S. 2019, arXiv:1904.02180
Stassun, K. G., Collins, K. A., & Gaudi, B. S. 2017, AJ, 153, 136
Stassun, K. G., & Torres, G. 2016, AJ, 152, 180
Stassun, K. G., & Torres, G. 2018, ApJ, 862, 61
Stassun, K. G., & Torres, G. 2021, ApJL, 907, L33
Stumpe, M. C., Smith, J. C., Catanzarite, J. H., et al. 2014, PASP, 126, 100
Stumpe, M. C., Smith, J. C., Van Cleve, J. E., et al. 2012, PASP, 124, 985
Tayar, J., Claytor, Z. R., Huber, D., & van Saders, J. 2022, ApJ, 927, 31
Teske, J., Wang, S. X., Wolfgang, A., et al. 2021, ApJS, 256, 33
Tokovinin, A. 2018, PASP, 130, 035002
Tokovinin, A., Fischer, D. A., Bonati, M., et al. 2013, PASP, 125, 1336
Torres, G., Andersen, J., & Giménez, A. 2010, A&ARv, 18, 67
Trotta, R. 2008, ConPh, 49, 71
Twicken, J. D., Catanzarite, J. H., Clarke, B. D., et al. 2018, PASP, 130, 064502
Wang, S., & Lin, D. N. C. 2023, AJ, 165, 174
Weiss, L. M., Isaacson, H. T., Marcy, G. W., et al. 2018, AJ, 156, 254
Weiss, L. M., Millholland, S. C., Petigura, E. A., et al. 2022, arXiv:2203.10076
Wolfgang, A., Rogers, L. A., & Ford, E. B. 2016, ApJ, 825, 19
Zechmeister, M., & Kürster, M. 2009, A&A, 496, 577
Zeng, L., Sasselov, D. D., & Jacobsen, S. B. 2016, ApJ, 819, 127
Zhou, G., Quinn, S. N., Irwin, J., et al. 2020, AJ, 161, 2
Zhu, W., Petrovich, C., Wu, Y., Dong, S., & Xie, J. 2018, ApJ, 860, 15
Ziegler, C., Tokovinin, A., Briceño, C., et al. 2020, AJ, 159, 19
Zink, J. K., Christiansen, J. L., & Hansen, B. M. 2019, MNRAS, 483, 4479